SANDIA REPORT

SAND2005-6797
Unlimited Release
Printed October 2005

Consequence Management, Recovery & Restoration after a Contamination Event

Scott C. James, Craig Jones, and Jesse D. Roberts

Prepared by
Sandia National Laboratories
Albuquerque, New Mexico 87185 and Livermore, California 94550

Sandia is a multiprogram laboratory operated by Sandia Corporation,
a Lockheed Martin Company, for the United States Department of Energy's
National Nuclear Security Administration under Contract DE-AC04-94AL85000.

Sandia National Laboratories

Issued by Sandia National Laboratories, operated for the United States Department of Energy by Sandia Corporation.

Available to DOE and DOE contractors from
U.S. Department of Energy
Office of Scientific and Technical Information
P.O. Box 62
Oak Ridge, TN 37831

Telephone: (865) 576-8401
Facsimile: (865) 576-5728
E-Mail: reports@adonis.osti.gov
Online order: http://www.doe.gov/bridge

Available to the public from
U.S. Department of Commerce
National Technical Information Service
5285 Port Royal Rd
Springfield, VA 22161

Telephone: (800) 553-6847
Facsimile: (703) 605-6900
E-Mail: orders@ntis.fedworld.gov
Online order: http://www.ntis.gov/help/ordermethods.asp?loc=7-4-0#online

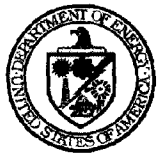

SAND2005-6797
Unlimited Release
Printed October 2005

Consequence Management, Recovery & Restoration after a Contamination Event

Scott C. James
Geohydrology Department

Craig Jones
SEA Engineering Inc.
200 Washington Street, Suite #210
Santa Cruz, California 95062

Jesse D. Roberts
Repository Performance

Sandia National Laboratories
P.O. Box 5800
Albuquerque, New Mexico 87185-0735

Abstract

The fate of contaminants after a dispersal event is a major concern, and waterways may be particularly sensitive to such an incident. Contaminants could be introduced directly into a water system (municipal or general) or indirectly (Radiological Dispersal Device) from aerial dispersion, precipitation, or improper clean-up techniques that may wash contamination into storm water drains, sewer systems, rivers, lakes, and reservoirs. Most radiological, chemical, and biological contaminants have an affinity for sediments and organic matter in the water system. If contaminated soils enter waterways, a plume of contaminated sediments could be left behind, subject to remobilization during the next storm event. Or, contaminants could remain in place, thus damaging local ecosystems. Suitable planning and deployment of resources to manage such a scenario could considerably mitigate the severity of the event. First responses must be prearranged so that clean-up efforts do not increase dispersal and exacerbate the problem.

Interactions between the sediment, contaminant, and water cycle are exceedingly complex and poorly understood. This research focused on the development of a risk-based model that predicts the fate of introduced contaminants in surface water systems. Achieving this goal requires integrating sediment transport with contaminant chemical reactions (sorption and desorption) and surface water hydrodynamics. Sandia leveraged its existing state-of-the-art capabilities in sediment transport measurement techniques, hydrochemistry, high performance computing, and performance assessment modeling in an effort to accomplish this task. In addition, the basis for the physical hydrodynamics is calculated with the EPA sponsored, public domain model, Environmental Fluid Dynamics Code (EFDC). The results of this effort will enable systems analysis and numerical simulation that allow the user to determine both short term and long-term consequences of contamination of waterways as well as to help formulate preventative and remedial strategies.

Acknowledgement

The research described in this document was funded through Sandia National Laboratories' Laboratory Directed Research and Development Program. Sandia is a multiprogram laboratory operated by Sandia Corporation, a Lockheed Martin Company, for the United States Department of Energy's National Nuclear Security Administration under contract DE-AC04-94AL85000.

Table of Contents

Abstract 3

Acknowledgement 4

Table of Contents 5

List of Figures 6

List of Tables 8

List of Tables 8

Introduction 9

Introduction 9

EFDC 11

EFDC Background 11

Non-cohesive sediments and effective particle size calculations 14

Effective size as the weighted arithmetic mean 14

Effective size based on weighted settling velocities 14

Effective size based on weighted critical shear velocities 15

Effective size as the weighted geometric mean 16

The Yen and Lee Experiments 16

Model Setup 16

Modeling results 18

Particle size data analysis 18

Evaluation of suspended load and bedload formulations 20

Evaluation of formulations based on effective particle size computed by different methods 22

Selection of optimal number of size classes 23

Conclusions – YL 24

SNL-EFDC 25

SEDZLJ Sediment Dynamics 25

Erosion 25

Erosion into Suspended Load vs. Bedload 27

Suspended Load 28

Bedload 30

Bed Armoring 32

The Little and Mayer Experiment 33

Model Setup 33

Model Results 34

Field-Tests 36

Lower Fox River 36

Model Setup 36

Model Results 36

Case 1 37

Case 2 38

Case 3 39

Cedar Lake 40

Model Set-Up 40

Model Results 42

Discussion and Conclusions 48

References 49

List of Figures

Figure 1: Settling velocity as a function of sediment grain size calculated with (5). 15

Figure 2: Critical Shields number as a function of grain size calculated with (10). 16

Figure 3: EFDC cell center locations (note that the figure has been rotated 90 degrees clockwise. 17

Figure 4: Relationship between flow rate and head above a 2.9-cm weir for the YL experiments. 18

Figure 5: Run 1 for bed topography (erosion) from (a) YL's Figure 2(a) and (b) EFDC. Here, the scale is $-2.1 \le \Delta z / h_0 \le 1.3$ and eight size classes with the Wu et al. (2000) bedload formulation is used. 21

Figure 6: Results from Run 1 for sediment gradation (sorting) from (a) YL's Figure 3(a) and (b) EFDC. Here, the scale is $0.5 \le d/d_0 \le 3.6$ and eight size classes with the Wu et al. (2000) bedload formulation is used. 22

Figure 7: Root mean squared error difference between erosion and sorting RMSE of the YL experiment and the EFDC model runs. 23

Figure 8: Comparison of modeled and experimental transport rates and change in average particle size over time. 35

Figure 9: (a) contour plot of the measured bathymetry used in SNL-EFDC and (b) modeled velocity vectors and corresponding bottom shear stresses. 37

Figure 10: Modeled results for Case 1. 38

Figure 11: Contour plot of total cesium concentration in the water column for Case 1. 38

Figure 12: Modeled results for Case 2. 39

Figure 13: Modeled results for Case 3. 40

Figure 14: Contour plot of cesium concentration remaining in the sediment bed for Case 3. 40

Figure 15: Three dimensional perspective of Cedar Lake bathymetry and grid. The vertical scale is exaggerated for clarity. 41

Figure 16: Cedar Lake bathymetry contours and east-west cross-sections for hydrodynamic evaluation. 42

Figure 17: Surface water velocity vectors and vertical velocity contours for a north wind. 43

Figure 18: Mid-water column velocity vectors and vertical velocity contours for a north wind. 44

Figure 19: Bottom water velocity vectors and vertical velocity contours for a north wind. 44

Figure 20: Velocity contours at Cross Section 1. 45

Figure 21: Velocity contours at Cross Section 2. 45

Figure 22: Velocity contours at Cross Section 3. 46
Figure 23: Bottom shear stress contours for a north wind. 47
Figure 24: Bottom shear stress contours for an east wind. 47
Figure 25: Bottom shear stress contours for a west wind. 48

List of Tables

Table 1: Values of the coefficients for (2). 13
Table 2: YL sediment size distribution. 20
Table 3: Single size class effective particle sizes for the YL data presented in Table 2. 20
Table 4: Suspended sediment information for each YL experimental run. 20
Table 5: RMSE comparisons between different bedload transport formulations for YL's Run 1. 21
Table 6: Erosion results based on different effective sizing techniques. 23
Table 7: Sediment size class properties. 34

Introduction

Quantifying the erosion and transport of contaminated sediment is critical for predicting contaminant fate and transport. Fine-grained, cohesive or mixed sediments are of particular interest because of the likelihood for contaminants to sorb onto them. The erosion characteristics of cohesive or mixed sediments can vary significantly with depth below the sediment-water interface as well as with applied shear stress. Furthermore, cohesive sediment erosion cannot be described using techniques similar to the well-established methods used for noncohesive sediment erosion because of the strength dependence of cohesive sediment on properties such as bulk density, mineralogy, pore water chemistry, organic content, etc. Although, researchers continue to advance the understanding of how these parameters affect cohesive sediment resuspension, a 'universal' formulation does not exist. Therefore, resuspension of fine-grained or mixed sediments is considered site specific and must be quantified independently for each site.

To adequately characterize the resuspension behavior of cohesive sediments, the current state of the art relies on *in-situ, ex-situ*, and laboratory measurements. A wide variety of devices may be used: flow-through flumes, re-circulating annular flumes, racetrack flumes, vertical jets, and vertically oscillating grids. Until the mid 1990s, contemporary erosion measurement devices were limited to surficial measurements (~ top 1 cm) under low flow conditions (not exceeding ~1 Pa). These limitations were overcome with the development of the SEDflume (McNeil, et al., 1996) in the Mechanical Engineering Department at the University of California at Santa Barbara. The SEDflume measures erosion: (a) with depth below the sediment-water interface (to account for consolidated and stratified sediments); (b) at high shear stresses (for flood and storm simulations); and, (c) in the laboratory or field (because the device is mobile).

Although the SEDflume was a major technical advance in erosion measurement devices, in the early 2000s, Sandia National Laboratories (SNL) developed the Adjustable Shear Stress Erosion and Transport (ASSET) Flume and the Sediment Erosion Actuated by Wave Oscillations and Linear Flow (SEAWOLF) Flume for performing *ex-situ* and laboratory analysis of sediment erosion and transport properties in current and combined current and wave dominated environments, respectively. Both devices are based on the proven SEDflume (McNeil, 1996) design and maintain all of the SEDflume's capabilities. The main difference between devices is that the ASSET Flume has been instrumented with bedload traps that afford simultaneous examination of transport modes (bedload vs. suspended load) of the eroded material. The SEAWOLF Flume applies an oscillatory flow across the sediment surface that can be superimposed upon a unidirectional current to re-create the shear history in combined wave-current environments such as the near shore areas of oceans and large lakes.

Advances in sediment erosion measurement devices brought about by the SEDflume, ASSET Flume, and SEAWOLF Flume have facilitated advances in sediment transport modeling. SNL has developed an integrated modeling tool to predict the mobility and fate of contaminants and contaminated sediments in surface water systems. Rather than building a model from first principles, SNL sought to expand and improve an existing model. Specifically, advances include incorporation of: (a) data read from output related to the SEDflume, ASSET and SEAWOLF Flumes; (b) chemical reaction kinetics; and, (c)

stochastic modeling techniques to facilitate uncertainty and sensitivity analyses of the model parameters in addition to probabilistic assessment of outcome scenarios.

Although several models are available for comprehensive modeling of flow and transport in river, ocean, and estuarine systems, the Environmental Fluid Dynamics Code (EFDC) developed for the U.S. Environmental Protection Agency (EPA, 2000) was selected for this work because it contains powerful hydrodynamic, water quality, and toxics solvers, while including its own sediment transport solver and several bed erosion formulations in one package. The hydrodynamic portion of the model solves the hydrostatic, free surface, Reynolds-averaged Navier-Stokes equations and turbulence closure, similar to the models of Blumberg and Mellor (1987) and Johnson et al. (1993). The numerical solution techniques are the same as those of Blumberg and Mellor (1987), except for the solution of the free surface that is done using a preconditioned conjugate gradient (direct) solver rather than an alternating-direction-implicit method. EFDC's pre-existing sediment transport algorithm is separated into noncohesive and cohesive transport boundary conditions and bed formulations, which does not lend itself to use of SEDflume data. Suspended load transport can be computed using a variety of formulations. For cohesive sediments, mechanisms include aggregation, settling, deposition, consolidation, and erosion. For noncohesive sediments, entrainment and deposition are determined by the excess Shields stress (van Rijn, 1984b) and sediment can be transported both as suspended load and bedload. Bedload fluxes may be computed with a variety of formulations, and an overall mass balance equation for the bedload is used to determine the removal or accumulation of material within a particular bed volume. Bed processes are computed using a conservation of sediment mass equation, the Exner equation (Parker et al., 2000) with an active layer, which is the layer closest to the overlying water. Several options are included in the model to quantify the above processes. The model also incorporates both linear and nonlinear forms of the Gibson equation for consolidation (Gibson et al., 1967), as well as an exponential formula for the density profile that was also developed by King et al. (2000).

Literature search and data evaluation led to the selection of EFDC for calculating the hydrodynamic of our sediment and contaminant transport dynamics model. EFDC includes cohesive and non-cohesive sediment transport sub-models, as well as a combined current-wave shear stress calculation and a layered sediment bed model; however, it handles cohesive and non-cohesive sediment erosion separately and not as a continuum. This is a major weakness because the majority of sediments in natural surface water systems are mixture of sand, silt and clay and the erosion process evolves continuously and both cohesive and non-cohesive sediment erode subjected to identical local shear stresses. To address this issue and also allow the incorporation of SEDflume (McNeil et al., 1996), ASSET flume (Roberts, et al. 2003), and SEAWOLF flume (Jepsen, et al. 2005) data into the model, Sandia selected the erosion and transport algorithms of the SEDZLJ (Jones et al., 2001) sediment and contaminant transport dynamics for further development and incorporation within the EFDC hydrodynamic model. The SEDZLJ model has been demonstrated for multiple applications to accurately simulate simultaneous cohesive and non-cohesive erosion, transport, and deposition of sediment mixtures as well as kinetic contaminant reactions. The new model is called SNL-EFDC.

As the precursor to a risk-based model that could predict the fate of contaminated sediments in surface water systems, several modeling experiments were performed to assess the existing capabilities of EFDC and more importantly to validate and demonstrate the capabilities of the newly developed SNL-EFDC. Initial work focused on modeling efficiency for noncohesive sediment mixtures that have wide ranges of particle sizes using the pre-existing sediment transport solver within EFDC. Model parameters are calibrated to a data set collected by Yen and Lee (1995), hereinafter referred to as YL. The best erosion formulation is determined. After the best erosion formulas have been selected to yield an acceptable match with experimental data, EFDC is used to simulate noncohesive sediment transport around a 180-degree curved waterway. A determination is made as to the number of particle sizes to include in the model that best reproduces the data. Four different techniques are proposed to calculate the effective particle size of a sediment sample. The effective particle sizing techniques are then evaluated by comparing model results to the YL data set. The required number of noncohesive sediment size classes is optimized to maximize computational efficiency. Finally, different numbers of sediment size classes are investigated with the goal of optimizing the number of size classes required for accurate assessment of model performance. This is assessed via statistical characteristics of sediment erosion and grain sorting.

Next, the experimental work of Little and Meyer (1972), hereinafter referred to as LM, provides an ideal data set for which to compare modeled erosion, bedload transport, and armoring (coarsening of the bed after erosion of the smallest sediment particles). SNL-EFDC was set up to simulate the LM experiment and the model results yielded an excellent approximation to the data without adjusting any model parameters.

Finally, real-world application of the SNL-EFDC model is presented for the Fox River, WI and Cedar Lake, IN. For the Fox River, SNL-EFDC was used to mimic a contamination event and determine the short-term spread and accumulation of contaminants within the model domain. For Cedar Lake, SNL-EFDC was used to determine the circulation patterns and resultant bed shear stress due to wind activity across the lake.

EFDC

EFDC Background

EFDC (Hamrick, 1996) incorporates hydrodynamics, salinity, temperature, dye, multiple size classes of cohesive and noncohesive sediments, toxicants, and water quality state variable transport into a comprehensive model. It is a three-dimensional model and is based on a curvilinear-orthogonal grid in the horizontal, and a sigma (or stretched) transformation in the vertical. It uses a finite volume-finite difference formulation to ensure conservation of mass. Water column transport is based on the same high-order advection-diffusion scheme used for salinity and temperature. A number of options are included for the specification of settling velocities. Sediment mass-conservative deposited bed formulations are included. The model had been applied at more than 60 project sites as of November, 2000.

For this work, EFDC appears to be the best choice of existing models because: (1) it has the same or similar hydrodynamic capabilities of the Princeton Ocean Model (Blumberg and Mellor, 1987) and ECOMSED (Shrestha et al., 2000); (2) it can represent inflows, and

has been modified to simulate nearshore areas (includes wetting and drying capabilities); (3) in addition to salinity and thermal transport, it can simulate multi-size sediment transport and the transport of equilibrium-partitioning toxic contaminants in both water and sediments; (4) it is EPA sponsored; and, (5) it can simulate nutrient cycling. The model has 20 state variables for simulating water column eutrophication and 26 state variables for simulating sediment biogeochemical processes. These characteristics provide the framework for addressing nutrient loading, but also provide options for applying the model to other water quality or toxic parameters (West Consultants, Inc., 1996).

In addition, the EFDC model has a number of other features that facilitate its use: (1) it has a user's manual and algorithm documentation; (2) it is non-proprietary; (3) it has a grid generator add-on, although any curvilinear orthogonal grid generator can be used; (4) it can run on many different types of computer platforms, including PCs; and, (5) it has a long history of application to estuary and riverine systems.

EFDC simulates the transport and fate of multiple size classes of cohesive and noncohesive suspended sediment, including bed deposition and resuspension. Hamrick (1996) provides an overview of the hydrodynamics. Noncohesive sediment may be transported as both bedload and suspended load depending on the flow conditions. Initiation of both modes of transport begins with erosion or resuspension of sediment i from the bed when the bed stress exceeds a critical stress referred to as the Shields stress, τ_{cr}. The Shield's stress depends upon the density and diameter of the sediment particles and applied shear stress and is defined as:

$$\theta_{cr_i} = \frac{\tau_{cr}}{\rho g' d_i} = \frac{u_{*_{cr}}^2}{g' d_i}, \tag{1}$$

which is also equal to the square root of the critical bed shear stress divided by the fluid density.

A number of approaches have been used to distinguish whether a particular sediment size is transported as bedload or suspended load under a specific local flow condition. The approach proposed by van Rijn (1984a) is adopted in EFDC. When the bed velocity is less than the critical shear velocity, $u_* < \left(g' d_i \theta_{cr_i}\right)^{1/2}$, no erosion or resuspension takes place and there is no bedload transport. Sediment in suspension under this condition will deposit to the bed. When the bed shear velocity exceeds the critical shear velocity, but remains less than the settling velocity, $u_{*_{cr_i}} < u_{*_i} < w_{s_i}$, sediment will be eroded and transported as bedload. Sediment in suspension under this condition will also deposit to the bed. When the bed shear velocity exceeds both the critical shear velocity and the settling velocity, bedload transport ceases and the eroded or resuspended sediment will be transported as suspended load.

EFDC allows the user to select from three empirical equations to specify the near-bed equilibrium noncohesive sediment concentration, or suspended load (and its corresponding reference distance above the bed), derived by Garcia and Parker (1991), Smith and McLean (1977), or van Rijn (1984b). The near-bed equilibrium sediment concentration is calculated as a function of hydrodynamic and sediment physical parameters. Because Garcia and Parker (1991) concluded that all three representations of near-bed sediment concentration

match reasonably well with experimental data and field observations, their formulation is used in all model runs discussed here because it is the newest and most comprehensive. Garcia and Parker's formulation is unique because it can account for armoring and hiding effects when multiple sediment size classes are modeled. Armoring occurs when the flow rate is sufficient to mobilize the smallest sediment particles, but insufficient to erode the largest particles. Hence, a portion of the bed erodes initially, but the erosion rate decreases as an increasing proportion of the surface layer sediments are large particles. Hiding is a similar type of phenomenon where large sediment grains hide smaller downstream grains from erosion.

EFDC also allows the user to select from five empirical formulations for the bedload transport rate (flux of noncohesive sediment from the bed), q_B [M/L^{2}T]. The equations follow the general form of

$$q_{B_i} = \rho_s \nu R_{d_i} \phi \left(\theta - \theta_{cr_i}\right)^{\alpha} \sqrt[\beta]{\theta}, \tag{2}$$

where μ [M/LT] is the absolute viscosity, α and β [–] are empirical constants, and ϕ is a function of critical Shields stress, θ_{cr}, and/or sediment grain Reynolds number, R_d, which is given by

$$R_{d_i} = \frac{d_i \sqrt{g' d_i}}{\nu}. \tag{3}$$

The formulations for (2) incorporated into EFDC are from Bagnold (1957), Engelund and Hansen (1967), Meyer-Peter and Müeller (1948), van Rijn (1984b), and Wu et al. (2000) and the corresponding coefficients are listed in Table 1. Sediment surface roughness should be calculated using the standard technique of Garcia (1999). YL's experimental data were used to determine which formulation for bedload transport rate best matched the laboratory results.

Table 1: Values of the coefficients for (2).

Reference	ϕ	α	β
Bagnold (1957)	7.6	1	1
Engelund and Hansen (1967)	$2.0367\left(\frac{H}{d_{50}}\right)^{1/3}\left(\frac{p_{e_i}}{p_{h_i}}\right)^{9/8}$ [a]	2.5	0
Meyer-Peter and Müeller (1948)	8	1.5	0
van Rijn (1984a)	$\frac{0.053}{R_d^{0.2}\theta_{cr}^{2.1}}$	2.1	0
Wu et al.(2000)	$\frac{0.053}{\left[0.03\left(\frac{p_{e_i}}{p_{h_i}}\right)^{-0.6}\right]^{2.2}}$	2.2	0

[a] p_{e_i} and p_{h_i} are the exposure and hiding probabilities of sediment d_i, respectively (see Wu et al., 2000), H is the depth of the water column, and d_{50} is the median sediment grain size.

Non-cohesive sediments and effective particle size calculations

Particle size analysis can be conducted using several techniques including sieving, electroresistance, X-ray, and laser diffraction. As long as particle sizing is performed under a consistent methodology, any method will provide information suitable for most model applications (Isphording et al., 2003). In this work, four techniques for calculating the effective sediment size are proposed. Each is used in EFDC model simulations of the experiments performed by YL to determine the effective size calculation technique that yields erosion results closest to the experimental data.

Effective size as the weighted arithmetic mean

The weighted arithmetic mean is simple to calculate, and the effective particle size is expressed as

$$d_{eff_A} = \frac{\sum_i f_i d_i}{\sum_i f_i}, \tag{4}$$

where d_i [L] is the particle size with volume fraction f_i [–]. The denominator in (4) is very close to unity with any discrepancy due to roundoff error. Up to a total of eight volume fractions are used in accord with the distribution reported by YL for their experiment.

Effective size based on weighted settling velocities

The settling velocity, w_{s_i} [L/T], is calculated for each volume fraction as (Soulsby, 1997)

$$w_{s_i} = \frac{\nu}{d_i}\left[\sqrt{10.36^2 + 1.049 D_*^3} - 10.36\right], \tag{5}$$

where the dimensionless particle diameter, D_* [–], is

$$D_* = d_i\left(\frac{g'}{\nu^2}\right)^{1/3}, \tag{6}$$

ν [L^2/T] is the kinematic viscosity, and buoyant gravity, g' [L/T^2] is

$$g' = g\left(\frac{\rho_s}{\rho_w} - 1\right), \tag{7}$$

where ρ_s [M/L^3] and ρ_w [M/L^3] are the sediment particle and water densities, respectively, and g [L/T^2] is gravitational acceleration. Once the settling velocities are calculated for each particle size, they are volume-fraction weighted to find the effective settling velocity

$$w_{s_{eff}} = \frac{\sum_i f_i w_{s_i}}{\sum_i f_i}. \tag{8}$$

The effective particle size is then calculated from the equation for settling velocity, (5), using Newton's method for solution of non-linear equations. Figure 1 illustrates the settling

velocity as a function of sediment particle size calculated by (5). Because of approximations used in its formulation, the equation for settling velocity should only be used for non-cohesive sediments (those with particle sizes greater than about 70 μm).

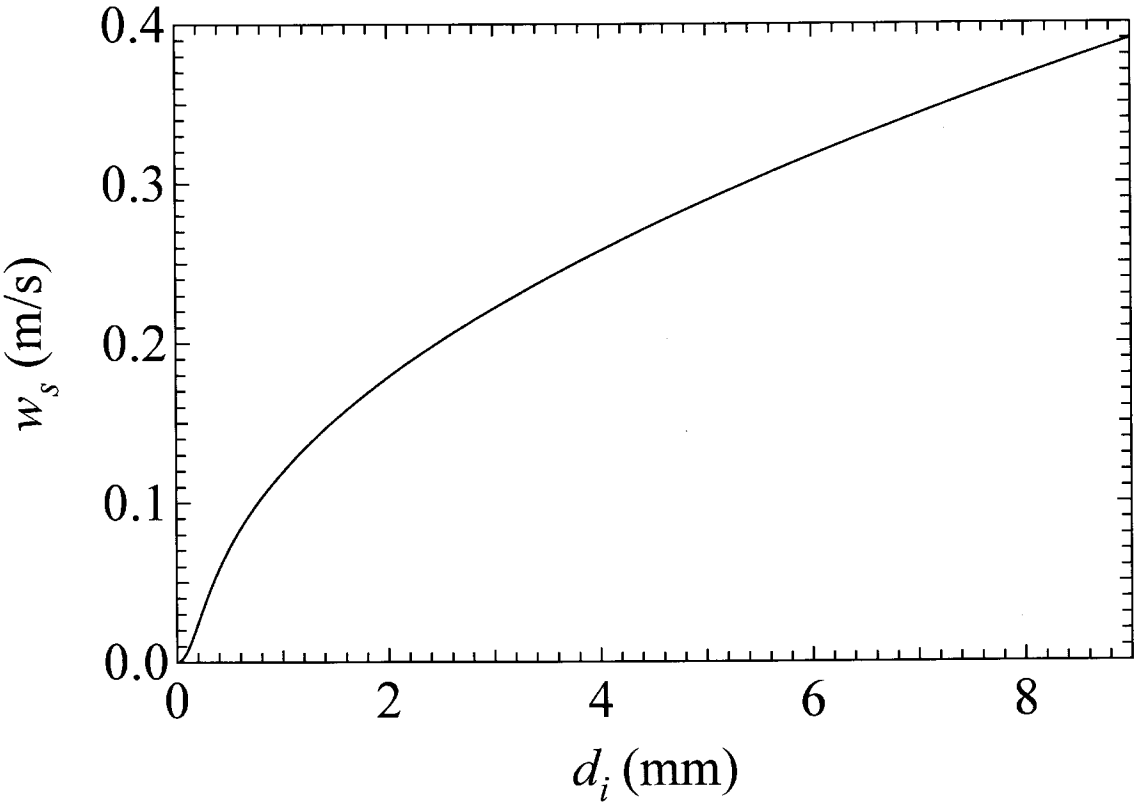

Figure 1: Settling velocity as a function of sediment grain size calculated with (5).

Effective size based on weighted critical shear velocities

The next technique used to calculate effective particle size is based on the weighted critical shear velocities of each size fraction. The critical shear velocity is expressed as (van Rijn, 1984a)

$$u_{*cr_i} = \sqrt{g' d_i \theta_{cr_i}}, \tag{9}$$

where the critical Shields number, which depends upon the density and diameter of the sediment particles and the kinematic viscosity of the fluid, is empirically approximated as (Soulsby, 1997)

$$\theta_{cr_i} = \frac{0.3}{1+1.2D_*} + 0.055\left[1-\exp\left(-0.02D_*\right)\right], \tag{10}$$

The effective critical shear velocity is the volume-fraction weighted critical shear velocity

$$u_{*cr_{eff}} = \frac{\sum_i f_i u_{*cr_i}}{\sum_i f_i}. \tag{11}$$

The effective diameter, d_{eff_U} [L], is calculated by linear interpolation over u_{*cr_i} [L/T] corresponding to different particle sizes. The critical Shield's number calculated with (10) as a function of sediment particle size is shown in Figure 2.

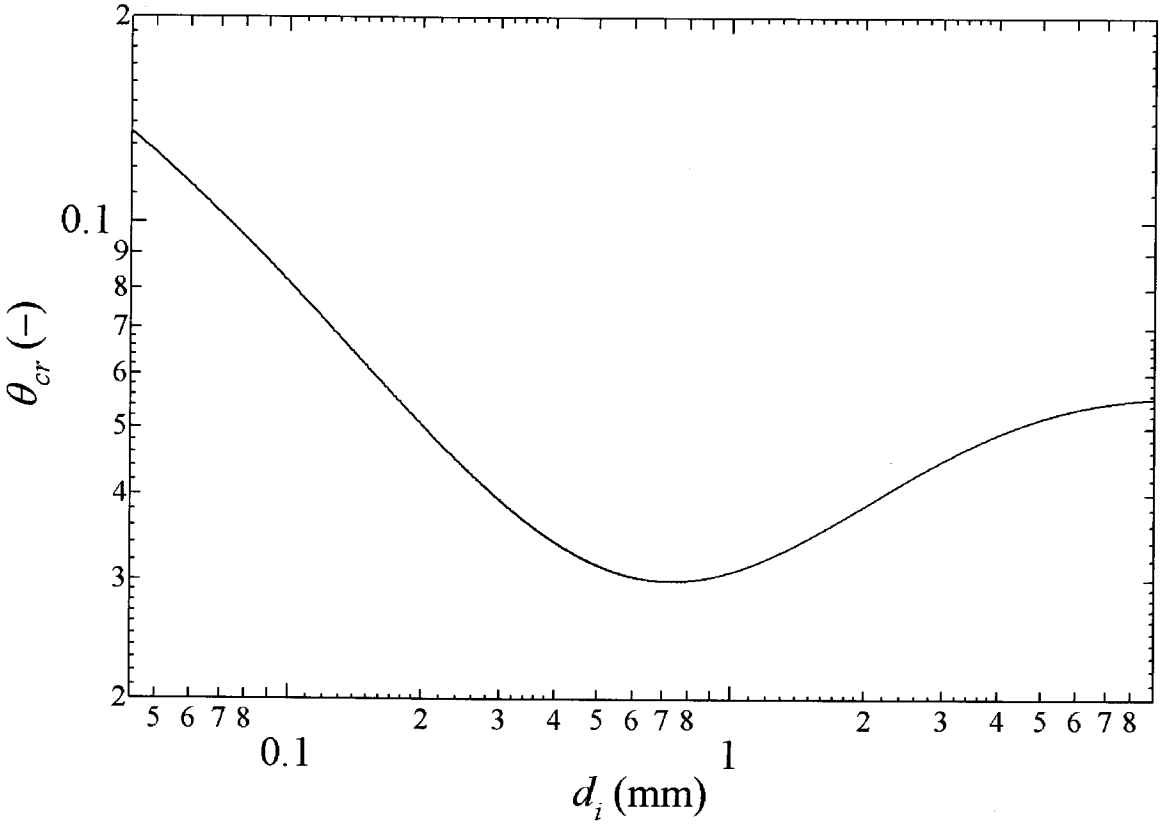

Figure 2: Critical Shields number as a function of grain size calculated with (10).

Effective size as the weighted geometric mean

The weighted geometric mean is easy to calculate, and the standard formulation is given by (Wikepedia, 2005)

$$d_{eff_G} = \prod_i d_i^{f_i}. \tag{12}$$

The Yen and Lee Experiments

Model Setup

The experimental work of YL is summarized here for completeness; however, the reader is referred to the manuscript of Yen and Lee (1995) for additional details. YL experimentally measured bed topography and sediment sorting in a channel bend subject to unsteady flow

conditions. This experiment provides an excellent backdrop for comparison to model results because it measures both non-cohesive sediment erosion and sorting in an unsteady flow regime. To summarize their experiment, 20 cm of noncohesive sand with known size gradation were placed in a laboratory channel bend with 11.5 m entrance and exit lengths, central angle of 180°, 4 m inner radius, and 1 m width. The channel was adjusted to a slope of 0.002 and base flow was 0.02 m^3/s (water depth of 5.44 cm) that increased linearly to a different maximum value for each run and then returned linearly to the base flow. A curvilinear orthogonal grid was developed to model the YL experiment with nine ζ- (x-)coordinates and 45 η- (y-)coordinates with cell centers as shown with blue dots in Figure 3. Eight sigma (z) levels were used along with eight sediment layers. The time step was specified as 0.05 s. The Mellor-Yamada level 2.5 turbulence closure scheme as modified by Galperin et al. (1988) is used to calculate turbulent flow in EFDC (Mellor and Yamada, 1982). The YL data (165 values each for erosion and sorting) were collected at point indicated by red dots in Figure 3. Erosion and deposition were modeled and measured as functions of bed elevation change with respect to the initial water depth, $\Delta z/h_0$. Sorting was calculated as the ratio final to initial median particle sizes, d/d_0. EFDC data were bi-linearly interpolated onto point coincident with the YL data for comparison of erosion and sorting.

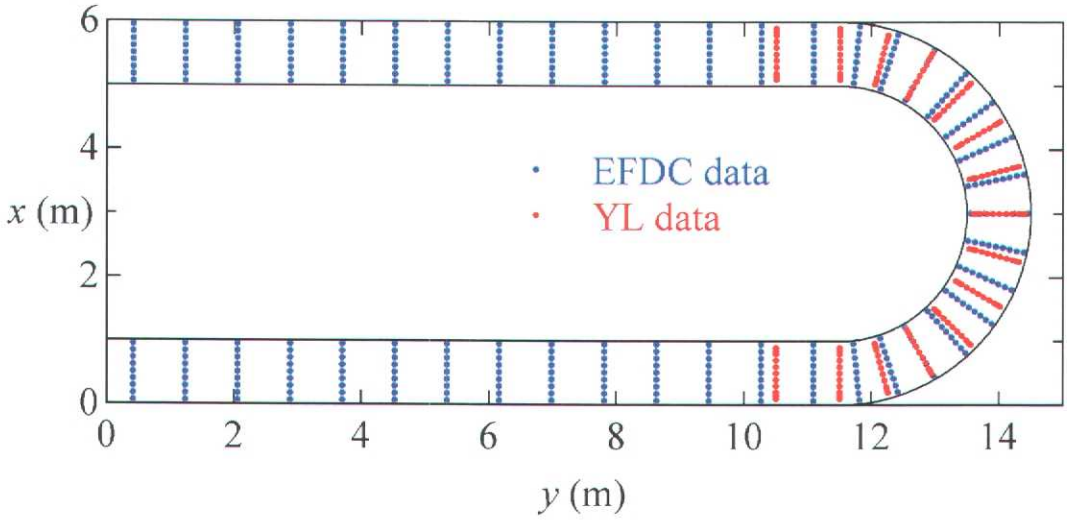

Figure 3: EFDC cell center locations (note that the figure has been rotated 90 degrees clockwise.

The weir equation was used to establish the weir height in the YL experiment, which is required to calculate the rating curve to be used as input to EFDC where the flow rate is specified as a function of depth (Franzini and Finnemore, 1997, Eq. 11.24)

$$Q = C_d \frac{2}{3} W \sqrt{2g} h^{3/2}, \tag{13}$$

where $W = 1$ m is the flume width, and h is the height of water (head) above the weir. The coefficient of discharge is given by the equation (Franzini and Finnemore, 1997, Eq. 11.25b)

$$C_d = 0.605 + \frac{1}{1000h} + 0.08\frac{h}{P}, \tag{14}$$

where P is the height of the weir. Data from YL (their Table 1) were used in a least-squares fit to specify $P = 2.9$ cm. This value yielded a correlation coefficient between the rating curve from (13) and the YL data of $R^2 = 0.997$. However, to perfectly correlate the EFDC input file with YL data, a polynomial was fit ($R^2 = 1$) to the data of Q vs. h with the calculated best-fit weir height of $P = 2.9$ cm yielding

$$Q = -579.14h^4 - 151.95h^3 - 11.89h^2 + 1.00h. \tag{15}$$

Because it is prudent to use all available data, (15) was used to specify the rating curve in EFDC instead of the weir equation. Figure 4 shows the relationship between flow rate and head above a 2.9-cm weir according to (13) and (15). Topography (erosion and deposition) and size sorting were carefully measured by YL at the conclusion of each run after the channel was slowly drained.

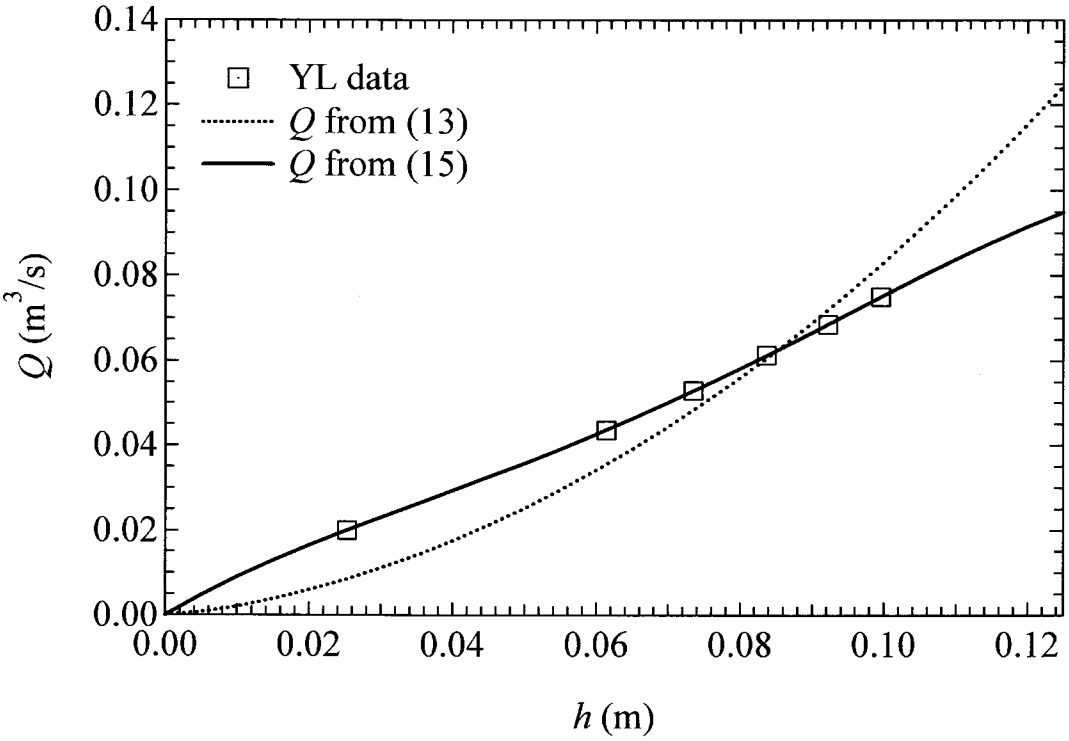

Figure 4: Relationship between flow rate and head above a 2.9-cm weir for the YL experiments.

Modeling results

Particle size data analysis

Using a single effective particle size to represent a distribution of sizes may be inappropriate for many natural sediments, particularly those with a large coefficient of uniformity (wide range in particle sizes) or multi-modal characteristics (two or more primary sizes). Thus, it may be suitable to replace a single effective particle size with

multiple effective particles sizes, each selected according to some size classification. While interpolating particle size distribution data could generate an infinite number of size classes, computational efficiency suggests that one should not increase, beyond what is necessary, the number of entities required to explain something. Certainly for model efficiency, there are a maximum number of size classes that should be used. Up to eight size classes, each with an effective particle size, are analyzed in this work based on the particle size distribution reported by YL, which was determined through a sieve analysis.

YL's particle size distribution is presented in Table 2. These data were sequentially transformed into fewer numbers of size classes, from eight down to one following the general size classifications of GARCIA (1999). The calculated single-size-class effective sizes using the four techniques described previously are listed in Table 3.

Table 2: YL sediment size distribution.									
d_i (mm)	0.10	0.25	0.42	0.84	1.19	2.00	3.36	4.76	8.52
f_i (–)	0	0.0655	0.1056	0.2536	0.1506	0.2011	0.1302	0.0488	0.0446

Table 3: Single size class effective particle sizes for the YL data presented in Table 2.				
Technique	d_{eff_A}	d_{eff_W}	d_{eff_U}	d_{eff_G}
Size (mm)	1.91	1.51	1.67	1.31

For the sediments in the five YL experimental runs, only sediment particles with $d_i = 0.25$ mm have the potential to travel as suspended load. This happens when the shear velocity exceeds both the critical shear velocity, (9), and the settling velocity, (5), for the particle size under consideration. The values for maximum particle size that may be suspended listed in Table 4 were calculated by equating settling velocities with shear velocities (the critical shear velocity is not a factor for these size particles: $u_{*_{cr}} \approx 0.014$ m/s while $0.033 < w_s < 0.042$ m/s) and solving for d_{max}. The maximum fraction of sediment that may be suspended, f_{max}, does not take into account the effects of armoring and hiding. These phenomena would tend to decrease f_{max}. In addition, Table 4 also indicates the number of minutes (and total percentage) of experiment time that 0.25 mm sediments may be suspended.

Table 4: Suspended sediment information for each YL experimental run.					
Experiment	Run 1	Run 2	Run 3	Run 4	Run 5
Experiment time (min)	180	204	240	300	420
Peak flow rate (m^3/s)	0.0750	0.0685	0.0613	0.0530	0.0460
d_{max} (mm)	0.301	0.297	0.290	0.282	0.272
(f_{max})	(0.0775)	(0.0766)	(0.0749)	(0.0730)	(0.0706)
Minutes that $d = 0.25$ mm can be suspended (% of experiment time)	157 (87%)	175 (86%)	170 (84%)	164 (81%)	150 (74%)

Evaluation of suspended load and bedload formulations

In YL's Figure 10, they present the sediment size distribution divided into eight size classes as shown in Table 2. Contour plots of EFDC-calculated bed thickness were compared to the experimental data of YL's Figure 2. In addition, contour plots of size ratios for both the model results and data were compared to illustrate sorting of larger particles to the outside of the bend and smaller particles to the inside. Physically, the helical flow generated around a bend mobilizes the smallest particles of the sediment toward the inside of the bend leaving the largest particles near the outside of the bend. Because the raw data from YL (Yen, 2004) do not match the EFDC grid spacing, a bi-linear interpolation scheme was used to compare model output to the data.

Simulations were conducted using the five empirical sediment bedload formulations listed in Table 1. Suspended loads in EFDC model results indicated that only the smallest size class, 0.25 mm, was found in suspension. Concentrations for this sediment at $5\text{ m} < x < 6\text{ m}$ and $y = 11$ m (at the outlet to the 180-degree bend) peaked at a value of 2.8 mg/L for Run 1, which is a negligibly small amount for these experiments. Because so little sediment was suspended in the experimental runs and corresponding numerical simulations, model output was not sensitive to the choice of suspended load transport formulation and any formulation could be used. The most

recently developed suspended sediment concentration formulation developed by Garcia and Parker (1991) was selected.

As expected, choice of bedload transport formulation significantly influenced model results. EFDC model outputs using the five different bedload transport formulations were compared to the results of experimental Run 1 by evaluating the root-mean-square-error (RMSE) of the bi-linearly interpolated model output and the experimental data (Yen, 2004). The RMSE is a rough measure of the standard deviation between modeled and measured results. As shown in Table 5, the Wu et al. (2000) formulation most closely matched the experimental data of YL because it had the lowest RMSE of all bedload formulations. Thus, this formulation was selected for all subsequent model simulations. Figure 5 shows $\Delta z/h_0$ erosion for both YL's Run 1 (see their Figure 2(a)) and EFDC results using eight size classes and the suspended load and bedload transport formulations indicated above. Figure 6 illustrates d/d_0 sorting for both YL's Run 1 (see their Figure 3(a)) and EFDC output. Qualitatively, EFDC yields results similar to the experimental data, although less outer bank erosion, more inner bank deposition, and greater size gradation are demonstrated in the model output. Overall, the results are accurate enough to lend confidence that the model correctly approximates natural erosion and gradation processes.

Table 5: RMSE comparisons between different bedload transport formulations for YL's Run 1.

Formulation	Bagnold (1956)	Engelund and Hansen (1967)	Meyer-Peter and Müeller (1948)	van Rijn (1984a)	Wu et al.(2000)
RMSE	0.80	0.66	0.86	0.81	0.52

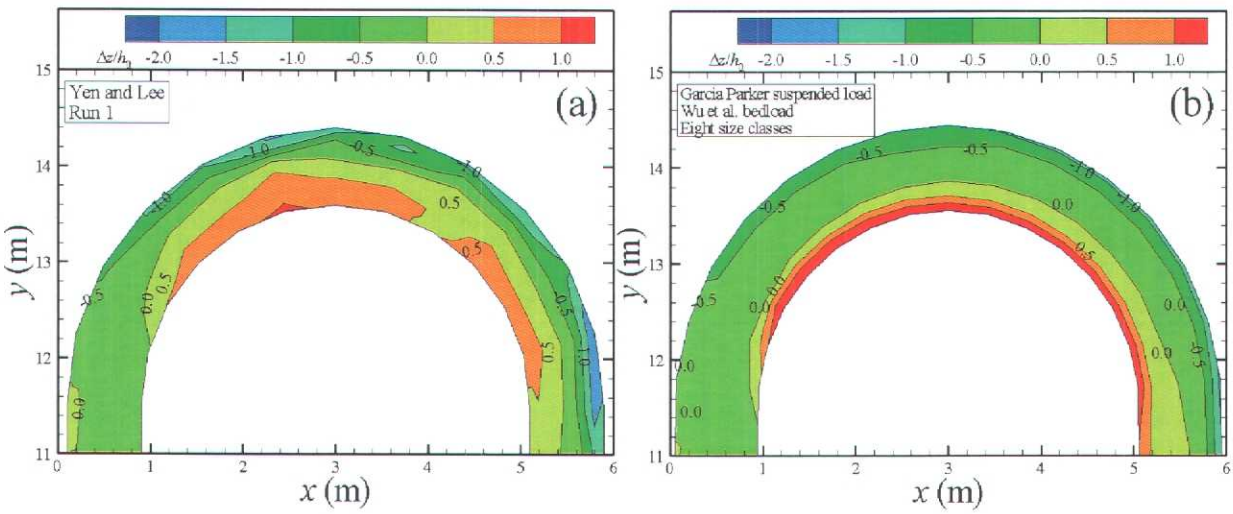

Figure 5: Run 1 for bed topography (erosion) from (a) YL's Figure 2(a) and (b) EFDC. Here, the scale is $-2.1 \le \Delta z / h_0 \le 1.3$ and eight size classes with the Wu et al. (2000) bedload formulation is used.

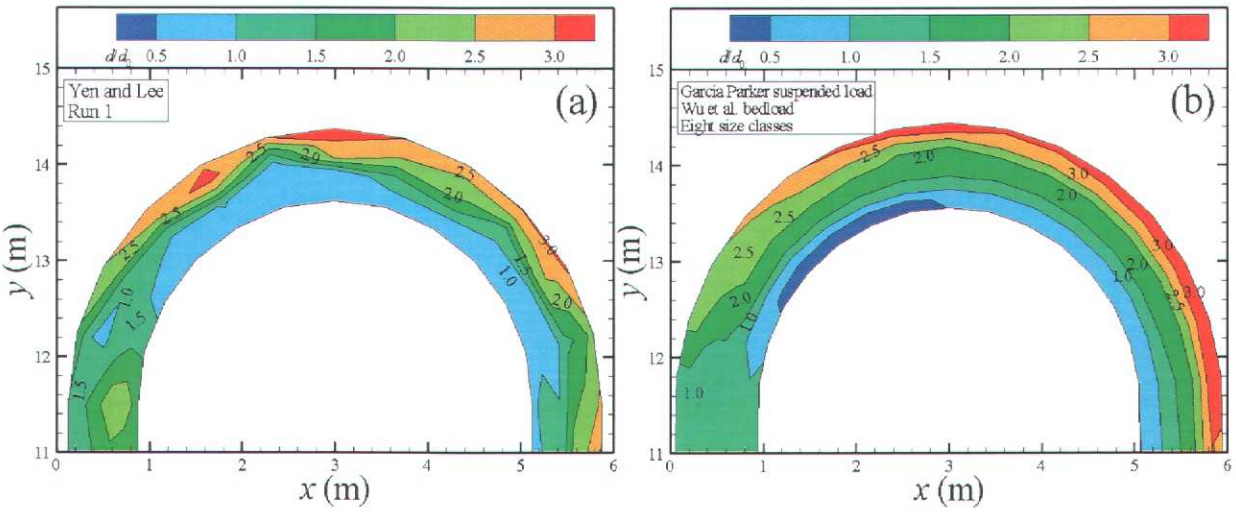

Figure 6: Results from Run 1 for sediment gradation (sorting) from (a) YL's Figure 3(a) and (b) EFDC. Here, the scale is $0.5 \le d/d_0 \le 3.6$ and eight size classes with the Wu et al. (2000) bedload formulation is used.

Evaluation of formulations based on effective particle size computed by different methods

The next phase of this study was to evaluate which of the single effective size formulations shown in Table 1 most closely matches the experimental data when using EFDC with the Wu et al. (2000) bedload formulation. Each RMSE listed in Table 6 was based only on measured and simulated erosion differences for all five experimental runs because there can be no sorting for only a single particle size class. The Average RMSE (i.e., the average across the five runs) is used as the metric for model accuracy. As shown in Table 6, using the different techniques to calculate a single effective particle size for EFDC simulations revealed that the effective particle size based on the geometric mean yields too much erosion, which results from it having the smallest effective size of all four techniques. Conversely, predicted erosion based on weighted arithmetic mean was typically less than that shown experimentally by YL because of the relatively large effective particle size. Based on the Average RMSE, the best effective sizing technique is to calculate particle size based on the weighted critical shear velocity. Although overall particle size based on the weighted critical shear velocity slightly outperforms that based on the weighted arithmetic mean, both techniques yield reasonable estimates of erosion and deposition for the YL experiments. Specifically, the weighted critical shear velocity yields better results for Runs 1, 2, and 3 while the weighted arithmetic mean yields more accurate results for Runs 4 and 5. RMSEs differ across Runs because of the varied experimental flows used (see Table 4) and the length of time that the prevailing shear stresses were above threshold for each experimental run. That is, for a single effective grain size, the numerical model will only allow erosion above the critical shear stress. However, in the experiment, there is a continuous distribution of grain sizes and therefore a distribution of critical shear stresses that initiate erosion (erosion of the smallest particles earlier in the experiment than in the numerical model). The inability of a single effective particle size to represent the distribution of critical shear stresses that yield significant erosion is likely the source of varied RMSEs between runs and sizing techniques. In addition, the differences may also be related to the exposure and hiding probabilities, and the ratio of grain roughness to channel bed roughness. The trend across runs

for each effective size calculation technique is as expected – there is less erosion and deposition as the peak flow for the run decreases.

Table 6: Erosion results based on different effective sizing techniques.

Sizing technique	RMSE Run 1	RMSE Run 2	RMSE Run 3	RMSE Run 4	RMSE Run 5	Average RMSE
d_{eff_A}	0.67	0.36	0.39	0.20	0.24	0.37
d_{eff_W}	0.14	0.25	0.25	0.65	0.74	0.41
d_{eff_U}	0.36	0.13	0.15	0.40	0.43	0.29
d_{eff_G}	0.32	0.61	0.63	1.10	1.19	0.77

Selection of optimal number of size classes

Because the goal of this work is to optimize the number of size classes in the model necessary to maintain reasonable agreement with experimental data, the eight size classes from YL were incrementally reduced down to two size classes and each model run was compared to the corresponding experimental run. Figure 6 is a plot of the RMSE for the differences between erosion and sorting for the YL and EFDC results. It should be noted that the weighted critical shear velocity was used to calculate effective particle sizes. Recall also that the Wu et al. (2000) bedload formulation [and the Garcia and Parker (1991) suspended load formulation] was used in all simulations because this erosion formulation most closely matched the experimental data when calibrating to Run 1 with eight size classes as shown in Figure 5a and 5b.

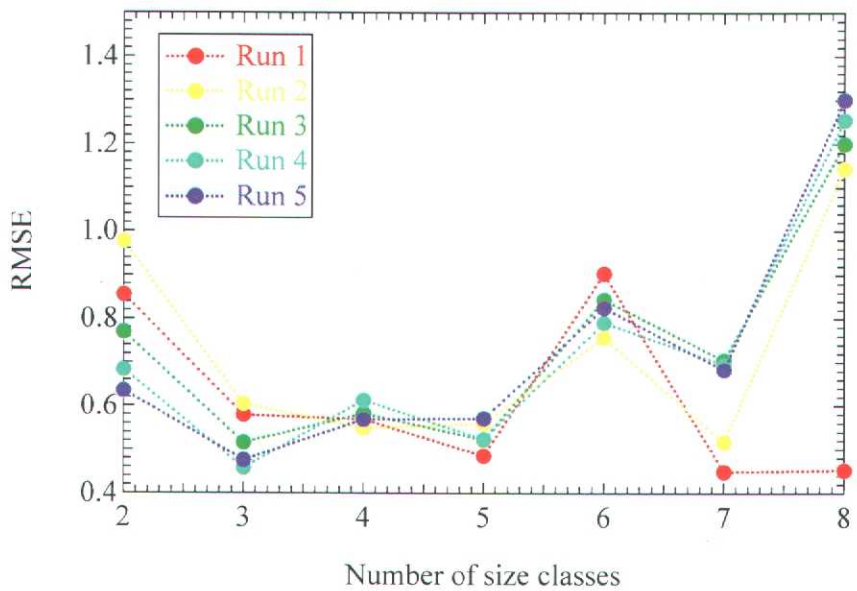

Figure 7: Root mean squared error difference between erosion and sorting RMSE of the YL experiment and the EFDC model runs.

In all model simulations, more erosion and deposition and less size sorting were evident, however there was a qualitative match to the experimental data. Accuracy between experimental and simulated results might be improved if other model parameters were varied (e.g., bed roughness, numerical solvers, turbulence closure schemes, etc.), but this was beyond the scope of this work. Note that the best match to YL topographic and size gradation data is for an EFDC run with three or five size classes because they share the minimum RMSE between experimental and model results. Unfortunately, no monotonic function relating the number of size classes to model accuracy could be found. That is, the values for erosion and size gradation in Figure 7 do not follow a simple linear relationship with the number of size classes. Interestingly, there is an oscillatory pattern of RMSE versus number of size classes, which is a result of the odd size classes matching the sorting better than even size classes. This happens because odd size classes always include an effective size class that is close to the median particle size. An important conclusion from this is that an odd number of size classes should always be used to model sediment erosion and gradation. Overall, results indicate that using three size classes for non-cohesive sediment in EFDC is optimum for matching the experimental data used here while minimizing processor time. It was noted that computation time increased approximately linearly with the number of effective size classes. On a Pentium IV, 3.4GHz machine, run times were approximately $1{,}237 + 815 \times$ (# of size classes) seconds.

One reason why RMSEs appear to diverge with increasing number of size classes is inherent in the way the model estimates erosion and in the necessity of discretizing sediment into particle size classes. As flow through the 180-degree bend increases, shear stress does as well. In addition, as the number of effective size classes in the model increases, the size of the smallest size class decreases from 1.7 mm for one size class to 0.25 mm for eight size classes. Because smaller sediment particles require less Shields stress to erode, an increase in the number of size classes will make more small size classes available to be eroded sooner and be transported farther. Therefore, it is expected that increasing the number of size classes in the model will generally increase the erosion potential of the sediment. Thus, when using multiple sediment particle size classes, other parameters like bed surface roughness or various turbulence closure schemes may need to be adjusted to improve model calibration.

Conclusions – YL

While it seems logical to include as many sediment size classes as possible in any modeling effort, a balance between model accuracy and computational expense, which increases with increasing number of size classes, must be achieved. In addition, the technique used to determine effective particle sizes should also be considered with respect to model accuracy. Using EFDC (not SNL-EFDC) to model non-cohesive sediment transport in a 180-degree bend subject to transient flow revealed that the combination of Garcia and Parker (1991) suspended load and Wu et al.(2000) bedload formulations yielded results most consistent with experimental data. Erosion and bed coarsening on the outside of the bend and deposition and bed fining on the inside were consistent with experimental results. Although more erosion and deposition and less size sorting were evident, model results qualitatively matched the experimental data. The influence of sediment sorting, relative roughness of grains with respect to channel roughness, and turbulence closure schemes inherent in the EFDC model need to be evaluated to further assess model performance. While modeling more size classes is increasingly computationally intensive, results from this study indicate that using three effective size classes to estimate the distribution of sediment particle sizes is optimum. In addition, when using only one size class in modeling (not

recommended) the best technique for calculating effective particle size is to simply use a weighted critical shear velocity.

SNL-EFDC

SEDZLJ Sediment Dynamics

Erosion

To quantitatively understand and predict the transport and fate of sediments and hydrophobic contaminants for a wide range of conditions, but especially during large floods on rivers and major storms on lakes and oceans when most sediment and contaminant transport occurs, it is necessary to accurately determine the erosion rates of sediments at different locations in the system, with depth in the sediments (often down to a meter or more), and at shear stresses up to and on the order of 25 N/m^2.

Erosion rates vary directly with the applied shear stress due to waves and currents, but are also complex functions of the bulk properties of the sediments. These rates often vary by orders of magnitude and in a non-uniform and non-predictable manner, both as a function of horizontal location and with depth. No general quantitative theory of sediment erosion rates valid for a wide range of conditions is available and, because of this, erosion rates must be measured.

To measure erosion rates at high shear stresses, with depth, and at different locations, a unique flume (called Sedflume) has been developed and applied (McNeil et al., 1996; Taylor and Lick, 1996; Jepsen et al., 1997; Lick and McNeil, 2001). Besides its use for field tests of relatively undisturbed sediments from cores, Sedflume has also been used in the laboratory to determine the effects of sediment bulk properties on erosion rates (Roberts et al., 1998; Jepsen et al., 2000).

A typical application of Sedflume yields erosion rates, E [LT^{-1}], as a function of depth with shear stress, τ. Erosion rates are generally highest at the surface and decrease with depth; they also increase with shear stress. These results will be used and discussed further below. For other cores, erosion rates can be a much more irregular function of depth than those shown here. In general, information of this type for sediments throughout the system is necessary for accurate predictions of sediment transport (Jones and Lick, 2000). Availability of this type of data is assumed and is used in the present model.

Information on erosion rates is generally reported in units of cm/s. To convert this to the mass flux in units of g/cm^2s required for modeling, the mass of solids within a sediment volume is needed. This quantity, for a sediment consisting of solids and water only (no gas), can be determined in terms of the bulk density of the sediments, ρ, as follows. Denote the density of solids as ρ_s, the volume fraction of the solids as x_s, the density of water as ρ_w, and the volume fraction of water as x_w. The bulk density is then given by

$$\rho = \rho_s x_s + \rho_w x_w, \tag{16}$$

$$= \rho_s x_s + \rho_w (1 - x_s), \tag{17}$$

because $x_w = 1 - x_s$. The mass of solids per unit volume is $x_s \rho_s$ and can be determined from the above equation as

$$x_s \rho_s = \frac{\rho_s(\rho - \rho_w)}{\rho_s - \rho_w}, \\ = \frac{2.6}{1.6}(\rho - 1), \tag{18}$$

where it has been assumed that ρ_s is 2.6 g/cm^3 and ρ_w is1.0 g/cm^3. Once the bulk density of the sediments is known, the erosion rate in units of g/cm^{2}s can be determined by multiplying the erosion rate in units of cm/s by $x_s\rho_s$.

As indicated above, erosion rates change as a function of depth. This variation is incorporated into the sediment bed model through a discrete layering system where the erosion rate is defined at each layer interface and the particle size distribution and bulk density are defined as constant throughout the layer. The number and thicknesses of the layers required to approximate the variation of sediment properties with depth can be determined from an inspection of the field data. The present model allows up to 15 layers with varying thicknesses. For the present studies, this is more than sufficient.

Because erosion rates are reported only for discrete shear stresses, a linear interpolation is used to calculate the erosion rate for the specified shear stress, τ^b, as

$$E(\tau^b) = \left(\frac{\tau_{m+1} - \tau^b}{\tau_{m+1} - \tau_m}\right) E_m + \left(\frac{\tau^b - \tau_m}{\tau_{m+1} - \tau_m}\right) E_{m+1}, \tag{19}$$

where the subscript m denotes data for a shear stress less than τ^b and $m + 1$ denotes data for a shear stress greater than τ^b.

Because E often changes rapidly with depth, a logarithmic interpolation between data points is used to calculate erosion rates as a function of depth,

$$\ln E(T) = \left(\frac{T_0 - T}{T_0}\right) \ln E^{\mathrm{L}+1} + \frac{T}{T_0} \ln E^{\mathrm{L}}, \tag{20}$$

where T is the layer thickness, T_0 [L] is the initial layer thickness, the superscript L denotes data for the interface at the top of the initial layer, and $L + 1$ denotes data for the interface at the bottom of the initial layer. Equations (19) and (20) can be combined so that the erosion rate can be determined as both a function of shear stress and depth.

In addition to erosion rates, another parameter of significance in modeling is the critical stress for erosion, τ_{ce}. This quantity can be understood and quantified as follows. Consider the flow of water over a sediment bed. As the rate of flow is increased starting from rest, there is a range of velocities (or shear stresses) at which the movement of the easiest-to-move particles (generally the smallest) is first noticeable to an observer. These eroded particles then travel a relatively short distance until they come to rest in a new location. This initial motion tends to occur only at a few isolated spots. As the flow velocity and shear stress increase further, more particles participate in this process of erosion, transport, and deposition, and the movement of the particles becomes more sustained.

Because of this gradual increase in sediment erosion as the shear stress increases, it is difficult to precisely define a critical velocity or critical shear stress at which sediment erosion is first

initiated. More quantitatively and with less ambiguity, a critical shear stress for erosion can be defined as the shear stress at which a small, but accurately measurable, rate of erosion occurs. In most previous studies, this rate is chosen to be 10^{-4} cm/s; this represents 1 mm of erosion in approximately 15 minutes, but more precision may be required for some applications.

As an example of this type of data, erosion rates and critical shear stresses for erosion of quartz particles of different sizes have been investigated by Roberts et al. (1998). For $d > 200$ μm, the sediments behave in a non-cohesive manner, i.e., they consolidate rapidly and they erode particle by particle. For $d > 1000$ μm, the critical shear stress shown agrees well with previous experimental data (e.g., see compilation of data by Miller et al., 1977) and can be approximated by

$$\tau_{ce} = 4.14d, \tag{21}$$

where τ_{ce} [$ML^{-1}T^{-1}$] is in N/m^2 and d [L] is in cm. For $d < 200$ μm, cohesive effects between particles become significant. The sediments consolidate relatively slowly with time, and the critical stresses depend not only on particle diameter but also on the bulk density of the sediments. For these cohesive sediments, τ_{ce} increases as d decreases and as ρ increases.

Erosion into Suspended Load vs. Bedload

As bottom sediments are eroded, a fraction of the sediments are suspended into the overlying water and are transported as suspended load; the rest of the eroded sediments move by rolling and/or saltation in a thin layer near the bed in what is called bedload. The fraction in each of the transport modes depends on particle size and shear stress.

For fine-grained particles (which are generally cohesive), erosion occurs both as individual particles and in the form of chunks or small aggregates of particles. The individual particles move as suspended load. The aggregates tend to move downstream near the bed but generally seem to disintegrate into small particles in the high stress boundary layer near the bed as they move downstream. These disaggregated particles then move as suspended load. For this reason, it is assumed here that fine-grained sediments less than about 200 μm are completely transported as suspended load. In contrast the statements above, preliminary experimental work with the ASSET Flume has indicated that for select sediments, fine-grained aggregates maintain their integrity with downstream transport. This work is ongoing and the concept of aggregate bedload transport is not currently incorporated within SNL-EFDC.

Coarser, non-cohesive particles (defined here as those particles with diameters greater than about 200 μm) can be transported both as suspended load and bedload, with the fraction in each dependent on particle diameter and shear stress. For particles of a particular size, the shear stress at which suspended load (or sediment suspension) is initiated is defined as τ_{cs} [$ML^{-1}T^{-1}$]. This shear stress can be defined from van Rijn's (1984b) formulations as

$$\tau_{cs} = \begin{cases} \rho_w \left(\dfrac{4w_s}{D_*} \right)^2 & \text{for } d \le 400\ \mu\text{m} \\ \rho_w \left(0.4 w_s \right)^2 & \text{for } d > 400\ \mu\text{m} \end{cases}, \tag{22}$$

where D_* is given by (6). For $\tau^b > \tau_{cs}$, sediments are transported both as bed load and suspended load with the fraction in suspended load, f, increasing with τ^b from $f = 0$ until f reaches 1. For τ^b greater than this, sediments are transported completely as suspended load.

Guy et al. (1966) have performed detailed flume measurements of suspended load and bedload transport for sediments ranging in median diameter, d_{50}, from 190 μm to 930 μm. They found that, as the ratio of shear velocity, defined as $u_* = (\tau^b/\rho_w)^{1/2}$, to settling velocity increases, the proportion of suspended load to total load transport, q_s/q_t, increases. An approximation of their data can be made with the following function:

$$\frac{q_s}{q_t} = \begin{cases} 0 & \text{for } \tau^b \le \tau_{cs} \\ \dfrac{\ln(u_*/w_s) - \ln\left(\sqrt{\tau_{cs}/\rho_w}/w_s\right)}{\ln(4) - \ln\left(\sqrt{\tau_{cs}/\rho_w}/w_s\right)} & \text{for } \tau^b > \tau_{cs} \text{ and } \dfrac{u_*}{w_s} < 4. \\ 1 & \text{for } \dfrac{u_*}{w_s} > 4 \end{cases} \qquad (23)$$

By multiplying the total erosion flux of a particular size class by q_s/q_t, the erosion flux of that size class into suspended load, E_s, can be calculated. The erosion flux into bedload, E_b, can be calculated by multiplying the total erosion flux of the size class by $(1 - q_s/q_t)$. Erosion fluxes for any size class k can be generally calculated with the expressions

$$\text{for } \tau^b \ge \tau_{ce,k} \begin{cases} E_{s,k} = \dfrac{q_s}{q_t}(f_k E) \\ E_{b,k} = \left(1 - \dfrac{q_s}{q_t}\right)(f_k E) \end{cases}, \qquad (24)$$

$$\text{for } \tau^b < \tau_{ce,k} \begin{cases} E_{s,k} = 0 \\ E_{b,k} = 0 \end{cases},$$

where f_k is the fraction by mass of the size class k in the surficial sediments.

Suspended Load

For suspended sediments, the two-dimensional (vertically integrated), time-dependent transport equation in the water over the bed is

$$\frac{\partial(hC_s)}{\partial t} + \frac{\partial(UC_s)}{\partial x} + \frac{\partial(VC_s)}{\partial y} = D_H\left[\frac{\partial}{\partial x}\left(h\frac{\partial C_s}{\partial x}\right) + \frac{\partial}{\partial y}\left(h\frac{\partial C_s}{\partial y}\right)\right] + Q_s, \qquad (25)$$

where C_s is the suspended sediment concentration and D_H [L^2T^{-1}] is the horizontal eddy diffusivity; D_H is determined from an empirical relation for rivers (Fischer et al., 1979), which is

$$D_H = 0.15\,h u_*, \qquad (26)$$

where h [L] is the local depth. If the transport model is numerically unstable at this value, D_H is increased until numerical stability is achieved. The net flux of sediments into suspended load

from the sediment bed, Q_s, is calculated as erosion flux into suspended load, E_s, minus the deposition flux from suspended load, D_s,

$$Q_s = E_s - D_s. \tag{27}$$

These equations are also valid for each size class k.

The suspended transport equations are converted into explicit finite difference equations that are second order accurate in space and time. The original numerical model for suspended sediments was developed by Ziegler and Lick (1986) and has been extensively verified by other researchers (Gailani et al., 1991; Cardenas et al., 1995; Chroneer et al., 1995).

An additional calculation must be made to calculate the suspended sediment concentration near the sediment bed for later use in calculating deposition. The suspended sediments do not always mix fully in the vertical. However, assuming a quasi-steady, one-dimensional balance between the settling and vertical turbulent diffusion of a particle, the concentration profile for each size class can be approximately determined to be

$$C_{sk}(z) = C_0 e^{-\frac{w_{sk} z}{D_v}}, \tag{28}$$

where C_0 is the near-bed concentration and D_v [L^2T^{-1}] is the vertical mass diffusivity calculated from an empirical relation for rivers (Fischer et al., 1979), which is

$$D_v = 0.067\, h u_*. \tag{29}$$

Equation (28) can be integrated over the water depth to yield a relation between the average suspended sediment concentration and the near-bed concentration. The near-bed concentration can then be determined directly at any location by using the average suspended sediment concentration from (18).

In a quiescent fluid where no shear stress is present, the deposition flux for suspended sediments can be described as the product of the settling speed of the sediment and the concentration of the sediment in the overlying water. However, in flowing water, the deposition is affected by the fluid turbulence, quantified as shear stress. In this case, a probability of deposition for each size class k, P_k, can be included in the formulation to account for the effects of the shear stress to yield

$$D_{sk} = P_k\, w_{sk}\, C_{sk}. \tag{30}$$

This probability would be unity in the case of quiescent flow and decrease as the flow, turbulence, and shear stress increase.

Suspended load deposition is calculated from the near-bed concentration obtained from (18). The probability for suspended load deposition seems to differ for cohesive and non-cohesive particle sizes. For cohesive particles, size classes with effective diameters less than 200 μm, Krone (1962) found that the probability of deposition varied approximately as

$$P_k = \begin{cases} 0 & \text{for } \tau^b > \tau_{cs} \\ \left(1 - \dfrac{\tau^b}{\tau_{cs}}\right) & \text{for } \tau^b \le \tau_{cs} \end{cases}, \tag{31}$$

For larger non-cohesive particles, size classes with an effective diameter greater than 200 μm, Gessler (1967) showed that the probability of deposition could be described with a Gaussian distribution, or error function given by

$$P_k = \text{erf}\left(\frac{Y}{2}\right), \tag{32}$$

where

$$Y = \frac{1}{\sigma}\left(\frac{\tau_{cs,k}}{\tau^b} - 1\right), \tag{33}$$

and $\tau_{cs,k}$ is the critical shear stress for suspension for size class k and σ is the standard deviation for shear stress variation, which was determined to be about 0.57.

An approximation to this function for $Y > 0$ with an error of less than 0.001 percent is (Dwight, 1961; Abramowitz and Stegun, 1972; HydroQual, Inc. 1997):

$$P_k = 1 - F(Y)\ \left(0.4632X - 0.1202X^2 + 0.9373X^3\right), \tag{34}$$

where

$$F(Y) = \frac{1}{(2\pi)^{1/2}} e^{-\frac{1}{2}Y^2}, \tag{35}$$

$$X = \left(1 + 0.3327\ \ Y\right)^{-1}. \tag{36}$$

When $Y < 0$,

$$P_k = 1 - P(|Y|), \tag{37}$$

This time, the settling speed is determined from the formulation of Cheng (1997), which is

$$w_s = \frac{\nu}{d}\left(\sqrt{25 + 1.2\,D_*^2} - 5\right)^{1.5}. \tag{38}$$

Because Cheng's formula is based on observations of the settling of real sediment particles, it produces settling speeds lower than Stokes' law. This is because real sediments are often irregular in shape and have a greater hydrodynamic resistance to settling than perfect spheres as in Stokes' law.

Bedload

For the description of bedload transport, van Rijn's (1984a) approach is used. To calculate the concentration of particles moving in bedload, a mass balance equation can be written as

$$\frac{\partial(h_b C_b)}{\partial t} = \frac{\partial q_{bx}}{\partial x} + \frac{\partial q_{by}}{\partial y} + Q_b, \tag{39}$$

where C_b is the bedload concentration, q_b is the horizontal bedload flux in the x or y directions, and Q_b is the net vertical flux of sediments between the sediment bed and bedload. This equation is solved using a central difference approximation for the fluxes in the x and y directions. The horizontal bedload flux in general is calculated as

$$q_b = u_b \, h_b \, w C_b, \tag{40}$$

where u_b [LT^{-1}] is the bedload velocity in the direction of interest, h_b [L] is the thickness of the bedload layer, and w [L] is the width of the area across which the flux is being calculated. The bedload velocity and thickness can be calculated from van Rijn's (1984a) formulations as

$$u_b = 1.5 \, T^{0.6} \left[(\rho_s - 1) g d \right]^{0.5}, \tag{41}$$

$$h_b = 3 \, d D_*^{0.6} \, T^{0.9}. \tag{42}$$

The transport parameter, T, is calculated as

$$T = \frac{\tau^b - \tau_{ce}}{\tau_{ce}}. \tag{43}$$

The flux of sediments between the bottom sediments and bedload, Q_b, is calculated as the erosion of sediments into bedload, E_b, minus the deposition of sediments from bedload, D_b, and is

$$Q_b = E_b - D_b, \tag{44}$$

where D_b is given by

$$D_b = P \;\; w_s C_b. \tag{45}$$

In steady state equilibrium, the concentration of sediments in bedload, C_e, is due to a dynamic equilibrium between erosion and deposition,

$$E_b = P w_s \, C_e. \tag{46}$$

From this, the probability of deposition can be written as

$$P = \frac{E_b}{w_s \, C_e}. \tag{47}$$

The erosion rate can be determined from Sedflume, while the settling speed can be calculated by (38). The equilibrium concentration, C_e, has been investigated by several authors; the formulation by van Rijn (1984a) will be used here and is calculated as

$$C_e = 0.117 \frac{\rho_s T}{d_*}. \tag{48}$$

Once E_b, w_s, and C_e are known as a function of particle diameter and shear stress, P can be calculated with (47). It is then assumed that this probability is also valid for the non-steady case so that the deposition rate can be calculated in this case also.

The equilibrium concentration, C_e, is based on experiments with uniform sediments. In general, the sediment bed contains and must be represented by more than one size class. In this case, the erosion rate for a particular size class is given by $f_k E_b$; it follows that the probability of deposition for size class k is then given by

$$P_k = \frac{f_k E_b}{w_{sk} f_k C_{ek}} = \frac{E_b}{w_{sk} C_{ek}}. \tag{49}$$

In this equation, it is implicitly assumed that there is a dynamic equilibrium between erosion and deposition for each size class k.

Bed Armoring

A decrease in sediment erosion rates with time, or bed armoring, can occur due to: (1) the consolidation of cohesive sediments with depth and time; (2) the deposition of coarser sediments on the sediment bed during a flow event; and, (3) the erosion of finer sediments from the surficial sediment, leaving coarser sediments behind, again during a flow event. The consolidation of sediments and subsequent change in erosion rates with depth can be determined by Sedflume in situ measurements. The consolidation of sediments and increase of erosion rates with time can be determined approximately from consolidation studies, again by means of Sedflume.

Here we are concerned about bed armoring due to processes (2) and (3). To describe these processes, it is assumed in the present model that a thin mixing layer, or active layer, is formed at the surface of the bed. The existence and properties of this have been discussed by previous researchers (Borah et al., 1983; van Niekerk et al., 1992; Parker et al., 2000). The presence of this active layer permits the interaction of depositing and eroding sediments to occur in a discrete layer without allowing deposited sediments to affect the undisturbed sediments below. Van Niekerk et al. (1992) have suggested that the thickness, T_a, can be approximated by

$$T_a = 2 d_{50} \frac{\tau^b}{\tau_{ce}}. \tag{50}$$

This formulation takes into account the deeper penetration of turbulence into the bed with increasing shear stress. In the present calculations, d_{50} is approximated by the average diameter in the interest of computational efficiency.

Because the active layer is kept at a constant thickness, T_a, three possible states of the active layer must be considered. The first state is a net erosion of the active layer, where there may be deposition occurring but the net flux is erosional. If the thickness of the active layer after this net erosion is T, then a thickness of material equal to $T_a - T$ is added to the active layer so that a thickness of T_a can be maintained. This material is added from the layer below in size class proportions equivalent to that in the layer below. The second possible state of the active layer is a net depositional state where the thickness of the active layer exceeds T_a. In this case, the excess material, $T - T_a$, is put into a new deposited material layer just below the active layer, but above the parent bed. This material is added to the deposited layer in size class proportions equal to the

active layer. The third state of the active layer is where T is equal in thickness to T_a. In this case, no action is taken.

The erosion rates for this active layer are dependent on its average particle size. As the particle diameter increases beyond 200 μm, the erosion rate decreases. This demonstrates how bed coarsening affects erosion rates. A dataset of this type can be constructed using laboratory and field cores to determine erosion rates as a function of particle size for any particular site. The erosion rate for an active or deposited layer can then be calculated from the average particle size of the layer with an interpolation similar to (20) with particle size in place of thickness.

The Little and Mayer Experiment

Model Setup

The evaluation and validation of the new model required comparison to a detailed and well-documented set of physical experiments. Non-cohesive sediment transport processes were evaluated against results of studies published by Little and Mayer (1972) and Yen and Lee (1995) because of their detailed measurements made within curved and straight open channel flumes, respectively.

The initial sediment distribution in the model was set equal to that in the respective flume experiments. Data from Roberts et al. (1998) studies on the erosion of quartz were used to define the erosion rates and critical shear stresses for erosion for the model.

The LM data set consists of surficial particle size distributions that were compared to the particle size distribution found in the active layer of the model. These results corresponded well and demonstrated the models ability to predict bed-coarsening phenomenon observed in many natural systems. The YL data set consists of contour plots of bed topography that demonstrate erosion and transport as well as size ratios that reveal sediment sorting. Comparative plots were created using the newly developed model outputs and a positive correlation was demonstrated.

To demonstrate the validity and application of the model proposed here, a comparison of the results from the model with results from a laboratory experiment was made. The LM flume studies of transport and bed coarsening in a straight channel provide an ideal dataset for this comparison. In their experiment, a flume 12.2 m long and 0.6 m wide was filled with a distribution of sand and gravel sediments. Clear water was then run over the sediment bed at a flow rate of 0.016 m^3/s. The eroded sediment was collected at the outlet of the flume, and the sediment transport rate was determined from this. When the sediment transport rate had decreased to 1 percent of the beginning transport rate, the bed was assumed to be fully armored and the experiment was ended. The full armoring of the sediment bed occurred in 75.5 hours. The final armored bed particle size distribution of the sediment surface was then measured by means of a wax cast.

This experiment was approximated with SNL-EFDC. Thirteen elements with a downstream dimension of 100 cm and cross-stream dimension of 60 cm were used to discretize the domain. The sediment bed comprised 9 size classes selected to accurately represent the sediment bed in the experiment. Table 7 shows the 9 size classes used in the model and their corresponding properties of settling speed, w_{s*}, critical shear stress for erosion, t_{ce*}, and critical shear stress for suspension, t_{cs*}. These nine size classes were selected to most closely correspond to the size distribution reported by LM. Data from the Roberts et al. (1998) Sedflume studies on quartz

were used to define the erosion rates and critical shear stresses for sediments in the model. The coefficient of friction was set such that the measured shear stress of 1.0 N/m^2 was reproduced in the model. The active layer was held at a constant thickness of 0.5 cm. Also, an upwind difference approximation was used to solve for the bedload transport, instead of a central difference approximation due to stability issues in this particular case.

Table 7: Sediment size class properties.

Particle size (μm)	Initial bed % (by mass)	w_s (cm/s)	τ_{ce} (N/m^2)	τ_{cs} (N/m^2)
125	2	0.9	0.15	0.15
222	8	2.25	0.24	0.26
432	23	5.2	0.33	0.45
1020	32	11.3	0.425	2.12
2000	11	18.01	0.93	5.36
2400	8	20.18	0.97	6.73
3000	6	23.07	1.2	8.79
4000	6	27.25	1.6	12.26
6000	4	34.13	2.48	19.2

Model Results

The model was run for 75.5 hr with a time step of 0.01 s. The model shows good agreement with the experimental data. In the first few hours, there is a rapid increase in the average particle size from 1,600 to 2,500 μm; this is followed by a much slower rate of increase to a little above 2,500 μm by the end of the experiment. Associated with this increase, is a four order-of-magnitude decrease in erosion rate. The reason for this decrease is that the finer particle sizes are eroded from the sediment bed while the coarser particles are left behind, thereby increasing the average particle size of the bed and decreasing the erosion rates. This is responsible for the drop in the net transport rate of sediments from the channel, and is consistent with bed coarsening as discussed earlier. The bedload and suspended load components of the total transport are shown in Figure 8. Initially the transport is almost equally bedload and suspended load, but as the bed coarsens the transport rate becomes almost exclusively bedload. This armoring process is expected since coarse particles, incapable of suspension at this shear stress, are mostly present in the bed.

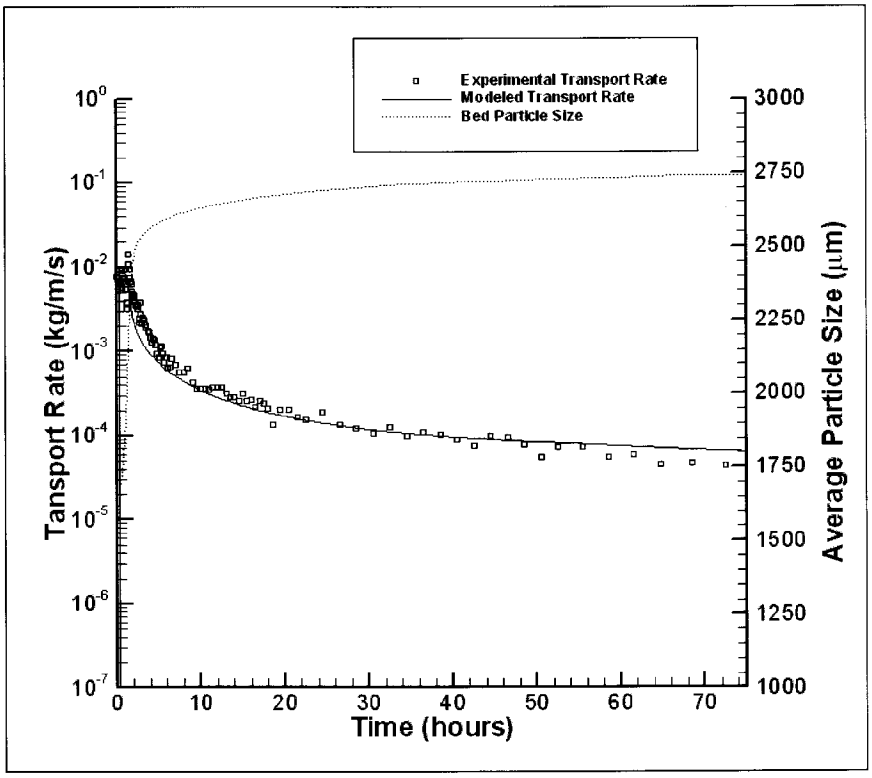

Figure 8: Comparison of modeled and experimental transport rates and change in average particle size over time.

A comparison is also made between the final particle size distribution in the active layer of the model and the particle size distribution of the surface of the bed in the experiment. Discrepancies between the two distributions are most evident at smaller particle sizes. Qualitatively both model and experiment show a significant amount of coarsening from the initial sediment bed. Discrepancies between the two distributions are most evident at smaller particle sizes. Although the distributions are not identical, the final d_{50} was 2,750 μm in the model and 3,200 μm in the experiment yielding a difference of 14 percent. One probable explanation for the difference in the two final distributions is that two different methods were used to obtain the distributions. The distribution obtained from the calculated 0.5-cm thick active layer (in which it is assumed that the sediments are uniformly distributed) might produce significantly different results from the surface wax casting method used in the experiment (which measures only the surface particles).

The results from this model show good overall agreement with the data and trends observed in the LM experiments. Such agreement indicates that the model accurately estimates the erosion, transport, and subsequent coarsening of a sediment bed.

The YL experiments have been re-modeled using SNL-EFDC, but results and interpretation are not available as of the time of this writing.

Field-Tests

Lower Fox River

Model Setup

The Lower Fox River was selected for field demonstration because it has been a well studied/characterized in recent years due to historical industrial contamination issues making it well suited for model evaluation. The model introduces a pulse of highly hydrophobic contaminant (Cesium) for six hours at its upstream boundary. The contaminant pulse was supplied at equilibrium between dissolved and particulate phases and comprised 10,000 g of Cesium. Three scenarios were considered:

1. An average flow rate of (105 m^3/s) and cesium partition coefficient, K_p = 1,000 L/kg,
2. An average flow rate of (105 m^3/s) and cesium partition coefficient, K_p = 10,000 L/kg,
3. A five year flood event (425 m^3/s) and cesium partition coefficient, K_p = 10,000 L/kg.

For each scenario tested significant localized areas of relatively high contamination remained within the model domain. Also, nearly the entire domain was contaminated to levels that would be considered unacceptable by EPA standards. The average flow scenarios allowed more sediment to deposit resulting in increased cesium residuals toward the edges of the river. A higher partition coefficient results in more cesium sorbed onto particulate material in the water column. Cesium associated with sediments may be transported or deposited depending on flow conditions.

Model Results

A Cartesian coordinate system derived from the model of Jones and Lick (2001) was used for the SNL-EFDC grid in the horizontal. Bathymetry data used to define the bottom of the lake are shown in Figure 9a. The modeled velocity vectors and corresponding bottom shear stress are shown in Figure 9b. Note that the narrow portion of the river corresponds to high velocities and shear stresses.

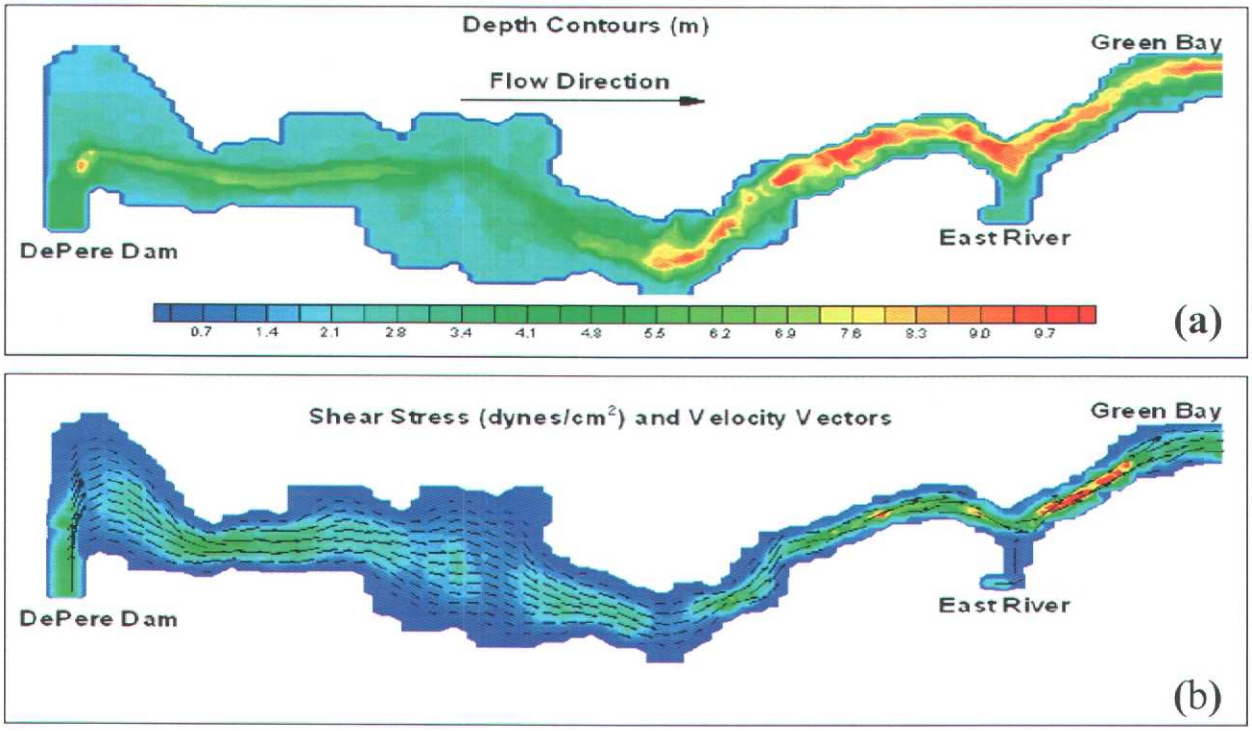

Figure 9: (a) contour plot of the measured bathymetry used in SNL-EFDC and (b) modeled velocity vectors and corresponding bottom shear stresses.

Case 1

Case 1 is a model for an average flow rate (105 m^3/s) and cesium partition coefficient (K_p = 1,000 L/kg) and results are shown in Figure 10. The long dashed curves is the total contaminant mass input to the system, the short dashed curves is the contaminant mass that has exited the system through the water column and associated with sediments. The solid curve is the mass in the sediment bed. Note that the model was not run to equilibrium as there is still some contaminant mass in the system (the sum of exited contaminant and contaminant in sediment do not equal the mass input to the system).

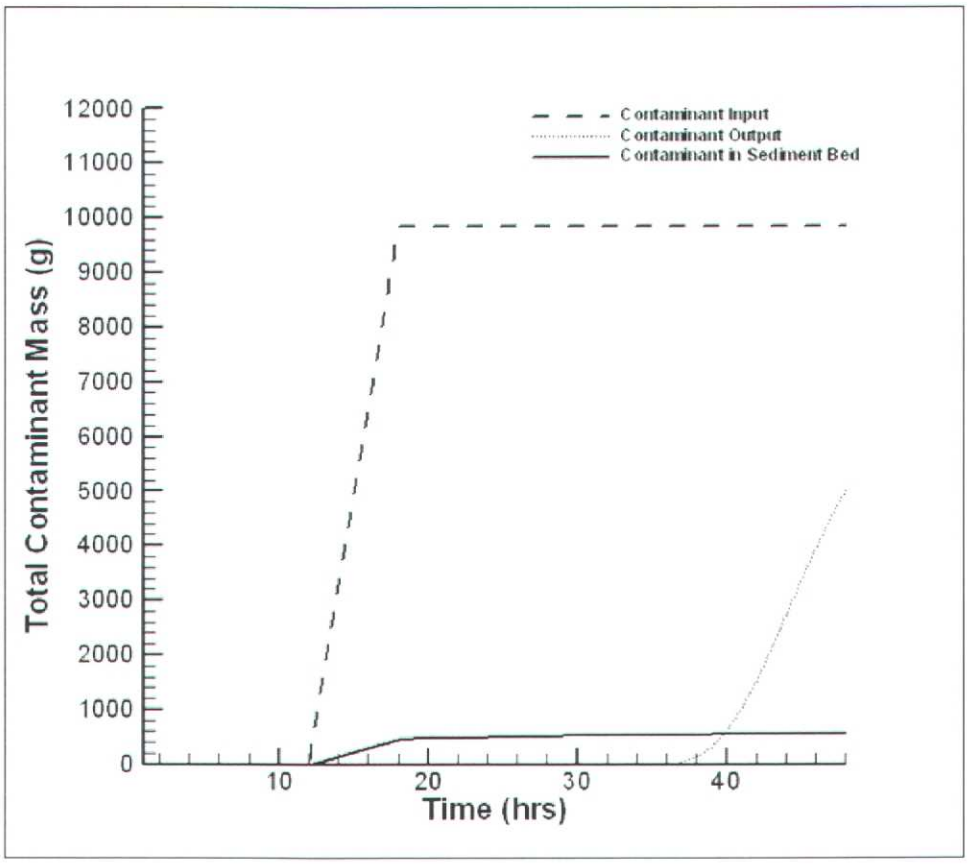

Figure 10: Modeled results for Case 1.

A contour plot of the total cesium concentration in the water column (dissolved and particulate) is illustrated in Figure 11 six hours into the release for Case 1. Cesium concentration is clearly affected by advection and dispersion.

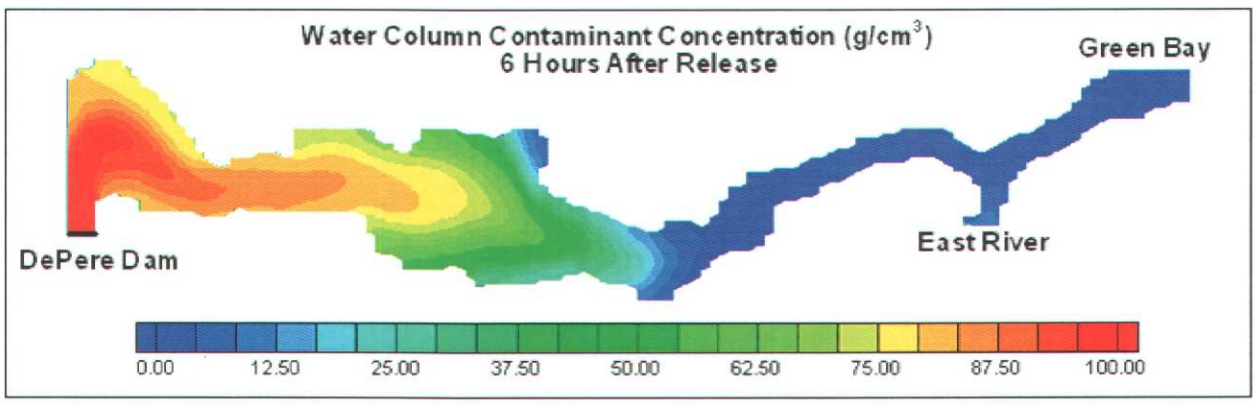

Figure 11: Contour plot of total cesium concentration in the water column for Case 1.

Case 2

Case 2 is a model for an average flow rate (105 m^3/s) and a high cesium partition coefficient (K_p = 10,000 L/kg) and results are shown in Figure 12. The long dashed curves is the total contaminant mass input to the system, the short dashed curves is the contaminant mass that has exited the system through the water column and associated with sediments. The solid curve is the

mass in the sediment bed. Note that with the higher partition coefficient that more contaminant mass is associated with sediments and remains in the river system.

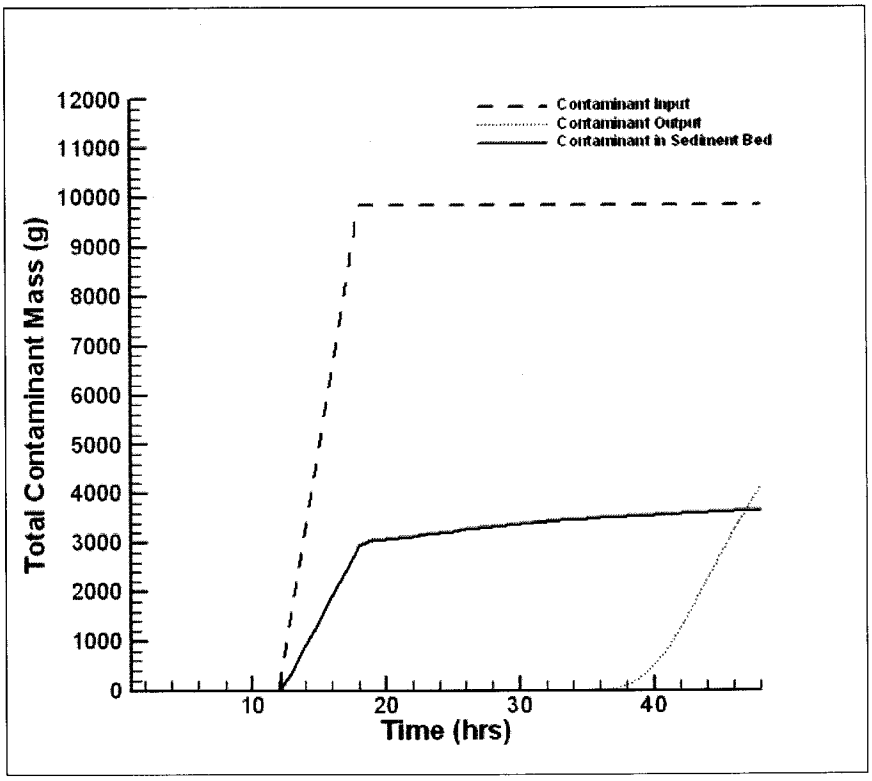

Figure 12: Modeled results for Case 2.

Case 3

Case 3 is a model for a once in five-year flood event (425 m^3/s) and a high cesium partition coefficient (K_p = 10,000 L/kg) and results are shown in Figure 13. The long dashed curves is the total contaminant mass input to the system, the short dashed curves is the contaminant mass that has exited the system through the water column and associated with sediments. The solid curve is the mass in the sediment bed. Again, the high partition coefficient yields more contaminant in the sediment bed compared to Case 1. But the high flow rate mobilizes more of the sediments, thus more cesium exits the system associated with sediments than in the other cases.

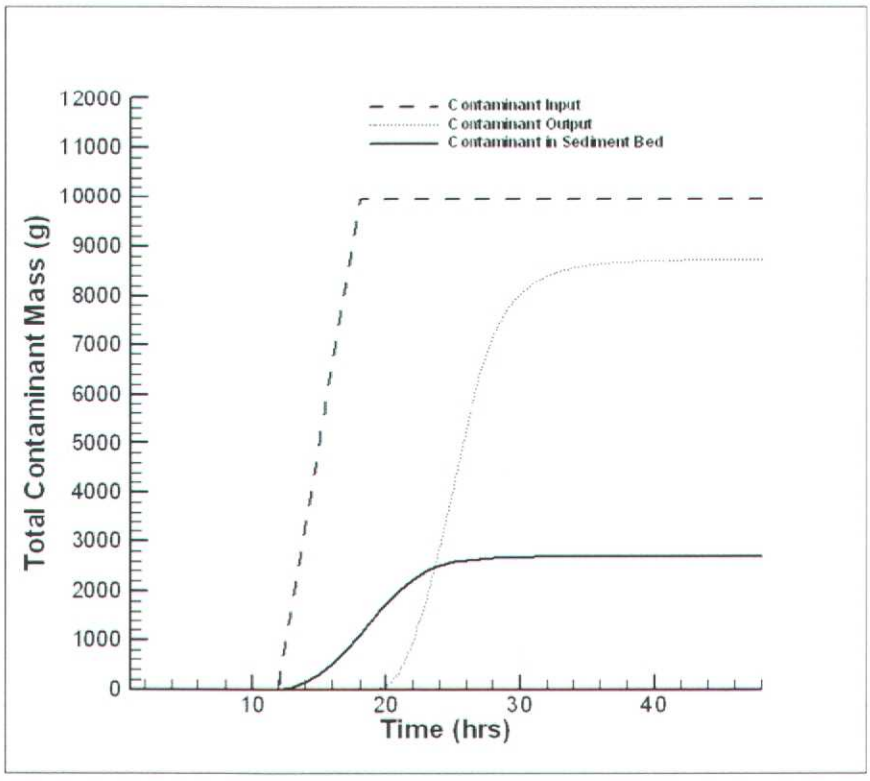

Figure 13: Modeled results for Case 3.

The final cesium concentration remaining in the sediment bed after the aqueous-phase pulse of cesium has exited the system is shown in Figure 14. Note the high (1 g/cm^3) concentration in areas where the velocity is low and less sediment erosion occurs. Also, the entire river bed is contaminated with levels higher than allowed by EPA regulations even in areas colored blue.

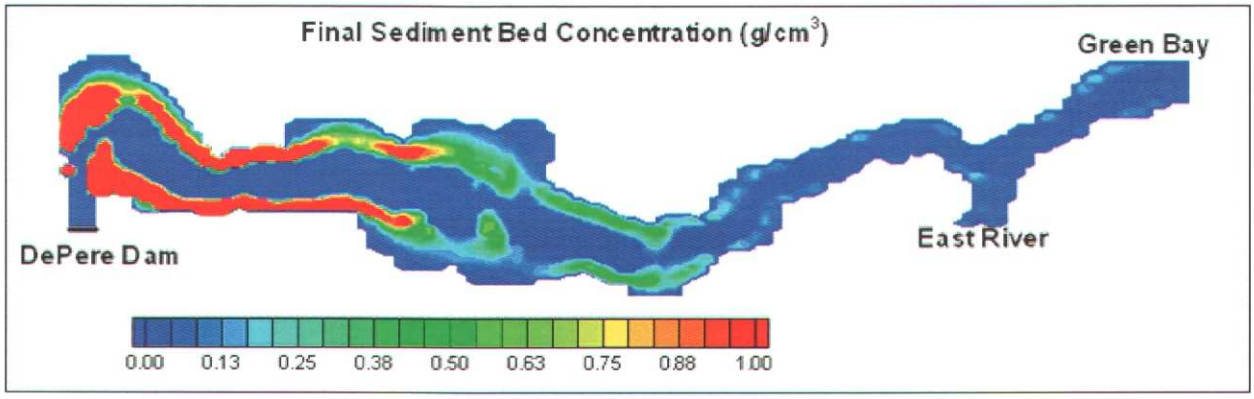

Figure 14: Contour plot of cesium concentration remaining in the sediment bed for Case 3.

Cedar Lake

Model Set-Up

The United States Army Corps of Engineers (USACE), Chicago District is performing a feasibility study authorized under the Section 206 of the Water Resources Development Act of 1996. The study will evaluate the feasibility of implementing aquatic ecosystem restoration

measures within Cedar Lake located in Northwest Indiana. This glacial lake experiences periodic resuspension of bottom sediments due to the hydrodynamic bottom stresses created by wind and boat activity. An associated release of phosphorus from the resuspension of bottom sediments is thought to be the main contributor to water quality degradation in the lake. As part of this feasibility study, the Chicago District is supporting the development of a water quality model within the lake to estimate and evaluate the effectiveness of potential ecosystem restoration measures.

The model of Cedar Lake, with bathymetry shown in Figure 15, was developed with SNL-EFDC. Cedar Lake has multiple small inlets and one outlet at several locations along the shoreline. None of these tributaries represent a major hydrodynamic forcing on the lake. In the absence of anthropogenic factors, wind driven circulation and wave action are the primary factors governing the hydrodynamic behavior of the lake. The average wind speed is 4.2 knots with an average direction out of the north-northeast. Wind speeds during storm events are sustained at up to 17 knots.

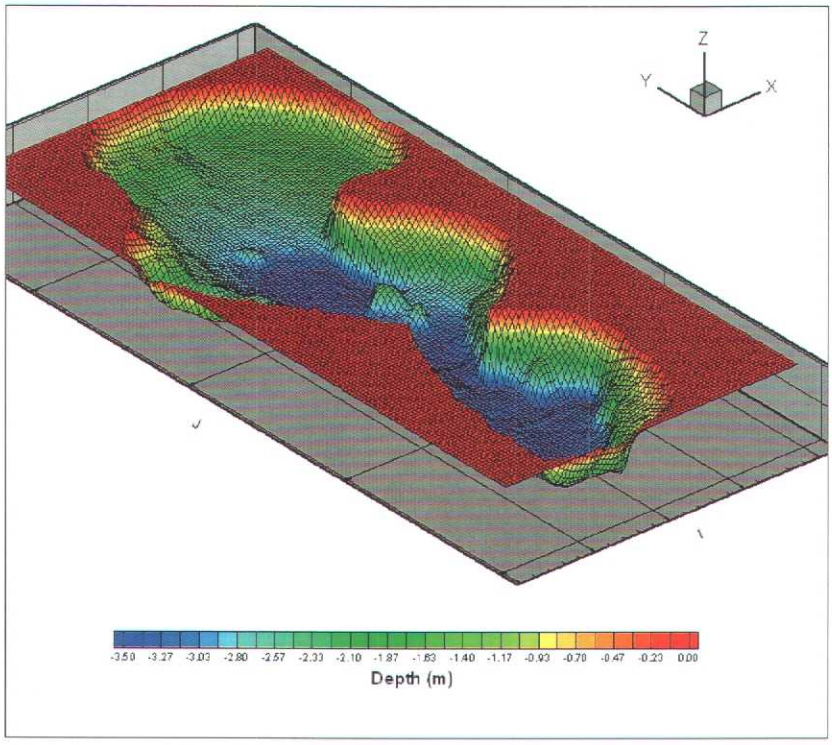

Figure 15: Three dimensional perspective of Cedar Lake bathymetry and grid. The vertical scale is exaggerated for clarity.

To simulate conditions under which sediment and contaminant transport would be the greatest, three scenarios representing the most likely storm wind and wave directions were simulated. These consisted of north, south and west winds of 17 knots. Analyzing the results from each scenario required consideration of horizontal slices of the lake at the surface, mid-water column, and the bottom of the lake and inspection of vertical cross sections of the lake with velocity contours with locations shown in Figure 16.

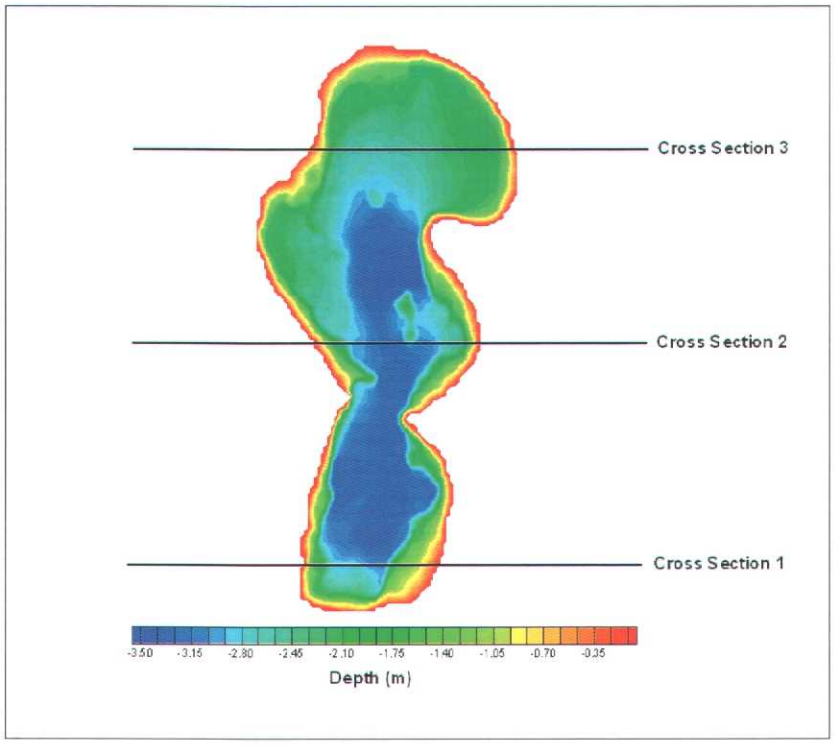

Figure 16: Cedar Lake bathymetry contours and east-west cross-sections for hydrodynamic evaluation.

Model Results

Considering a north wind of 17 knots we observe at the lake surface, the net movement of water is southward from the wind out of the north. The velocities are largest near the shorelines in shallow water. At the mid-water column, a return flow to the north is seen in the central lake region to balance the southward flow of water at the surface. Additionally, downward velocities are seen along the south shore and upward velocities are seen along the north shore. Additionally, vertical circulation is also seen at the narrow central portion of the lake. The bottom of the lake also shows a notable flow to the north, which again balances the southward flow at the surface of the lake. The shallow nearshore regions show a strong southerly flow while the deeper portion of the lake shows the return flow to the north. The south flow due to the wind is again seen to be highest near the surface while the return flow is highest near the bottom. The circulation observed due to a strong wind across the axis of the lake is characteristic of wind-driven circulation on lakes observed worldwide (Fisher et al., 1979).

To investigate sediment and contaminant transport, it is necessary to calculate the hydrodynamic shear stress exerted on the bottom of the lake due to currents and waves. Waves were incorporated into the model using wave heights and periods calculated from the wind speed and direction of interest. The model computes total shear stress due to all combined hydrodynamic forces. This is the shear stress responsible for the resuspension of lake sediments. Conversely, the currents alone are responsible for the water column transport of sediments and contaminants.

For each wind direction, the highest shear stresses are seen along the downwind shoreline of the lake where the combined wave heights and current speeds are the largest. The maximum shear stresses generated in the lake rarely exceed 0.2 Pa. Preliminary sediment analyses indicates that

surficial critical shear stresses of the sediments are between 0.05 and 0.10 Pa, meaning that sediment resuspension and contaminant recycling could be initiated in several areas of the lake.

To simulate conditions under which sediment and nutrient transport would be the greatest, three scenarios representing the most likely storm wind and wave directions were simulated. The first case is a north wind of 17 knots. Figure 17–19 show horizontal slices of the lake at the surface, mid-water column, and the bottom of the lake. The slices show velocity vectors whose length is a function of magnitude and vertical velocity contours. The blue in the contours represents negative or "downward" vertical velocities while the red contours represent positive or "upward" vertical velocities. The vertical velocities approach zero at the surface and the bottom of the lake.

At the lake surface, the net movement of water is southward from the wind out of the north. The velocities are largest near the shorelines in shallow water. At the mid-water column, a return flow to the north is seen in the central lake region to balance the southward flow of water at the surface. In addition, downward velocities are seen along the south shore and upward velocities are seen along the north shore. Furthermore, vertical circulation is also seen at the narrow central portion of the lake. The bottom of the lake also shows a notable flow to the north which again balances the southward flow at the surface of the lake.

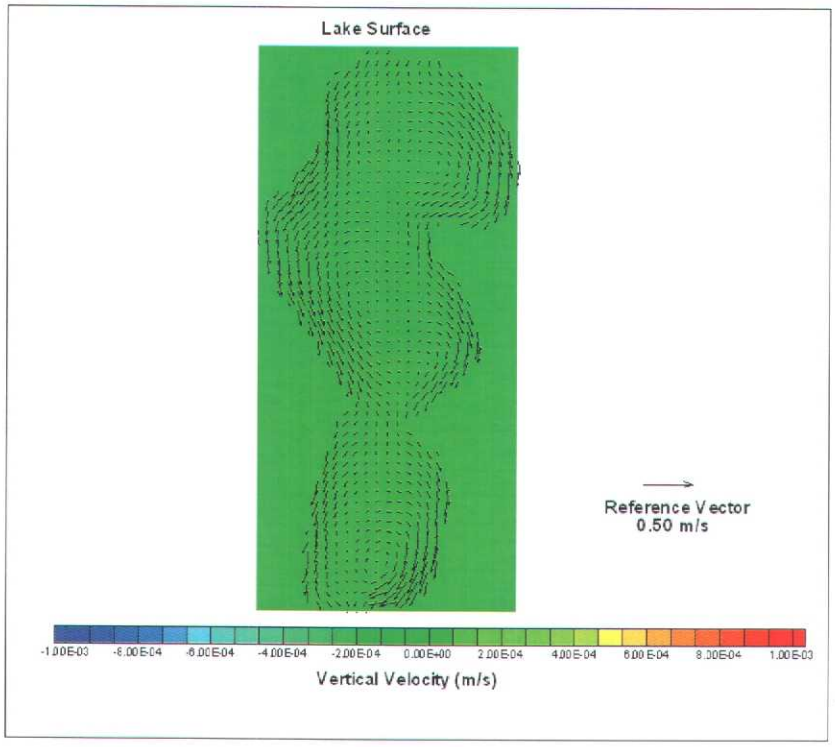

Figure 17: Surface water velocity vectors and vertical velocity contours for a north wind.

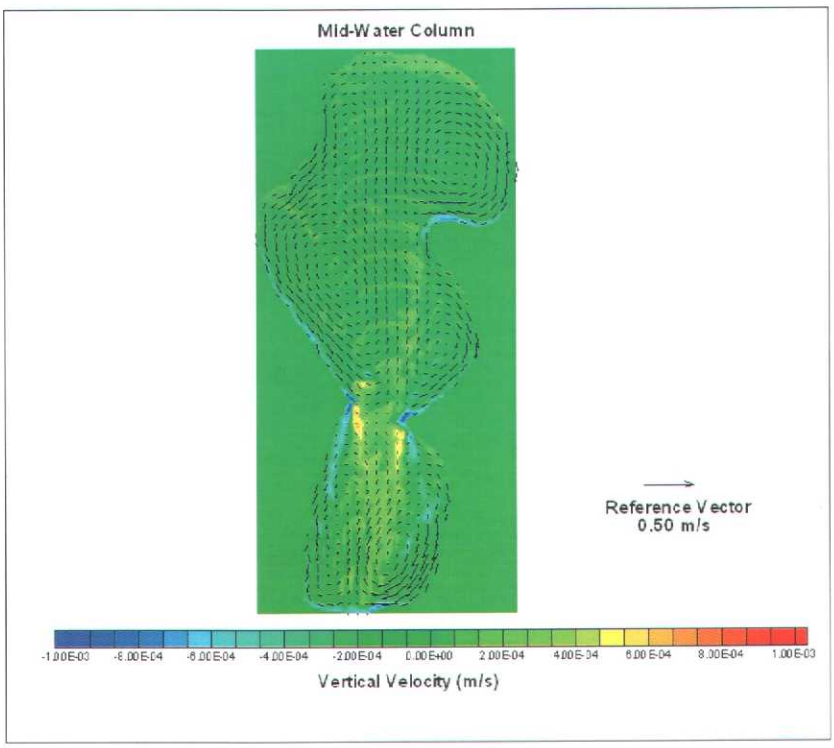

Figure 18: Mid-water column velocity vectors and vertical velocity contours for a north wind.

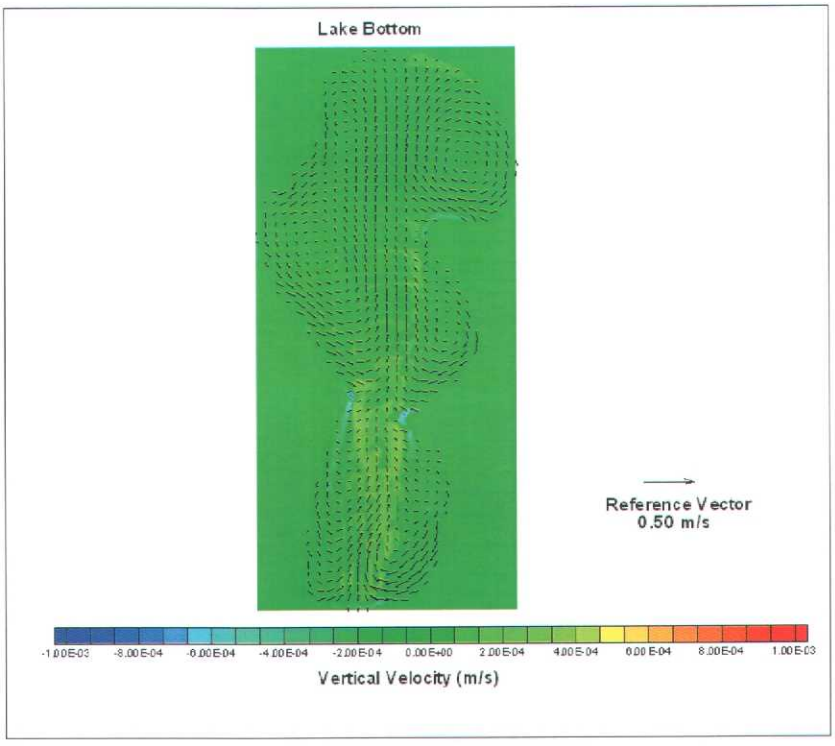

Figure 19: Bottom water velocity vectors and vertical velocity contours for a north wind.

Figure 20–22 show vertical cross sections of the lake with velocity contours. The velocity contours are the magnitude of the north - south velocity with blue indicating south velocities (out of the page) and red indicating north velocities (into the page). The shallow nearshore regions

show a strong southerly flow while the deeper portion of the lake shows the return flow to the north. The south flow due to the wind is again seen to be highest near the surface while the return flow is highest near the bottom. The circulation observed due to a strong wind across the axis of the lake is characteristic of wind-driven circulation on lakes observed worldwide (Fisher et al., 1979).

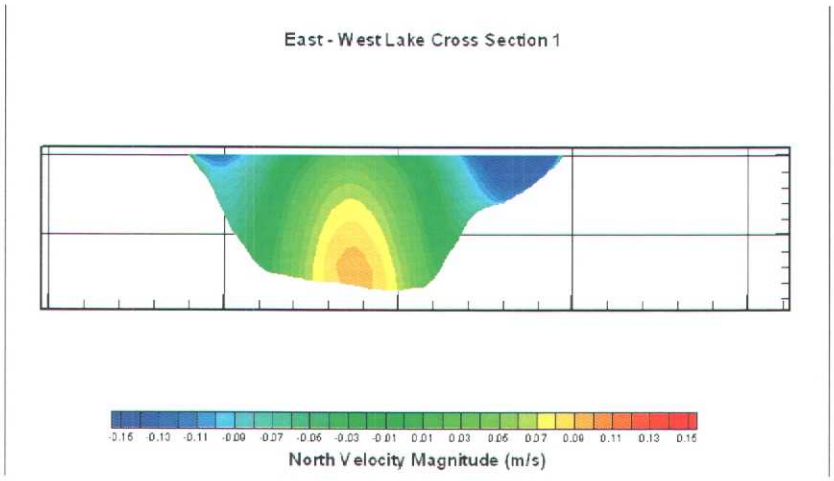

Figure 20: Velocity contours at Cross Section 1.

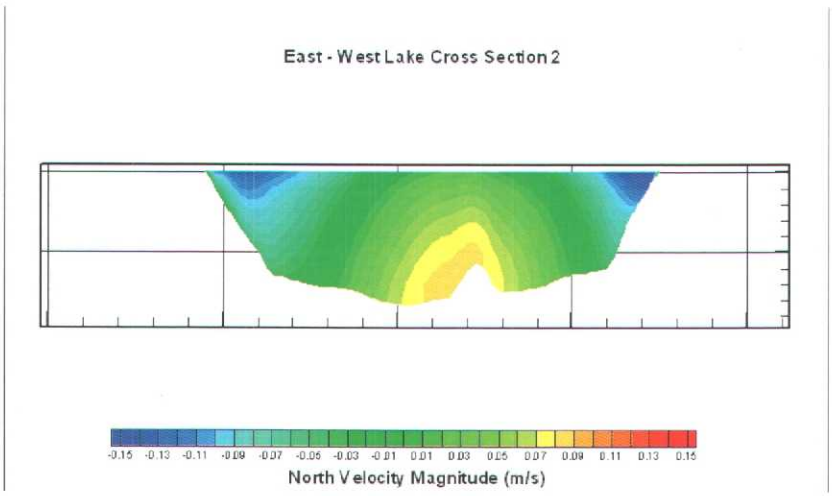

Figure 21: Velocity contours at Cross Section 2.

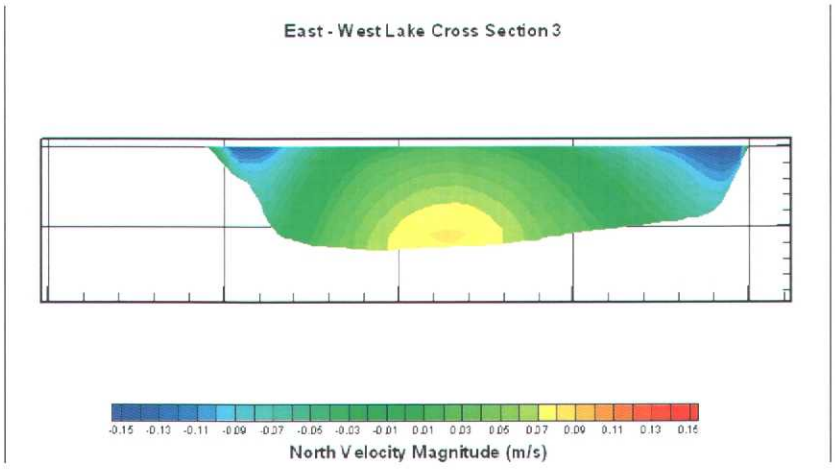

Figure 22: Velocity contours at Cross Section 3.

To investigate sediment and nutrient transport, it is necessary to calculate the hydrodynamic shear stress exerted on the bottom of the lake due to currents and waves. Waves were incorporated into the model using wave heights and periods calculated from the wind speed and direction of interest. The USACE Coastal Engineering Manual (CEM) standard methodology for fetch limited wave growth was used to calculate the wave characteristics. These values were distributed to the model grid for each wind direction simulated.

Once the waves were mapped onto the model grid, the current and wave vectors were used to calculate the bottom shear stresses throughout the lake using the Grant and Madsen (1979) wave and current boundary layer model. The model computes total shear stress due to all combined hydrodynamic forces. This is the shear stress responsible for the resuspension of lake sediments. Conversely, the currents alone are responsible for the water column transport of sediments and nutrients.

Figure 23–25 show the bottom shear stress contours in Pascals (Pa) in the lake for the three dominant wind directions (north, east, and west). For each case, the highest shear stresses are seen along the downwind shoreline of the lake where the combined wave heights and current speeds are the largest. The maximum shear stresses generated in the lake rarely exceed 0.2 Pa. Preliminary sediment analyses indicated the lowest surficial critical shear stresses of the sediments to be approximately 0.15 Pa, meaning that sediment resuspension is initiated in the red contoured areas for each case.

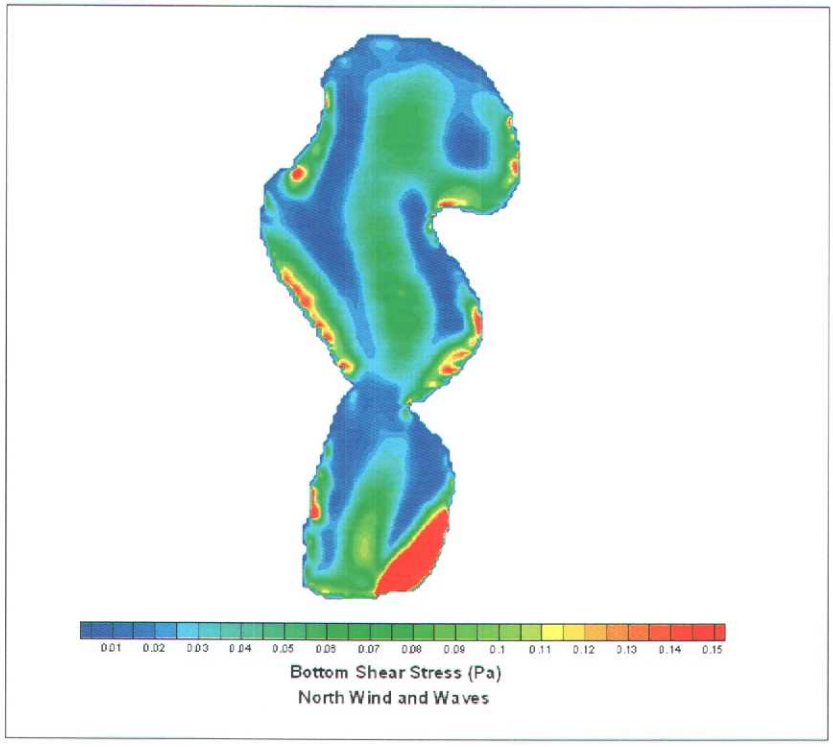

Figure 23: Bottom shear stress contours for a north wind.

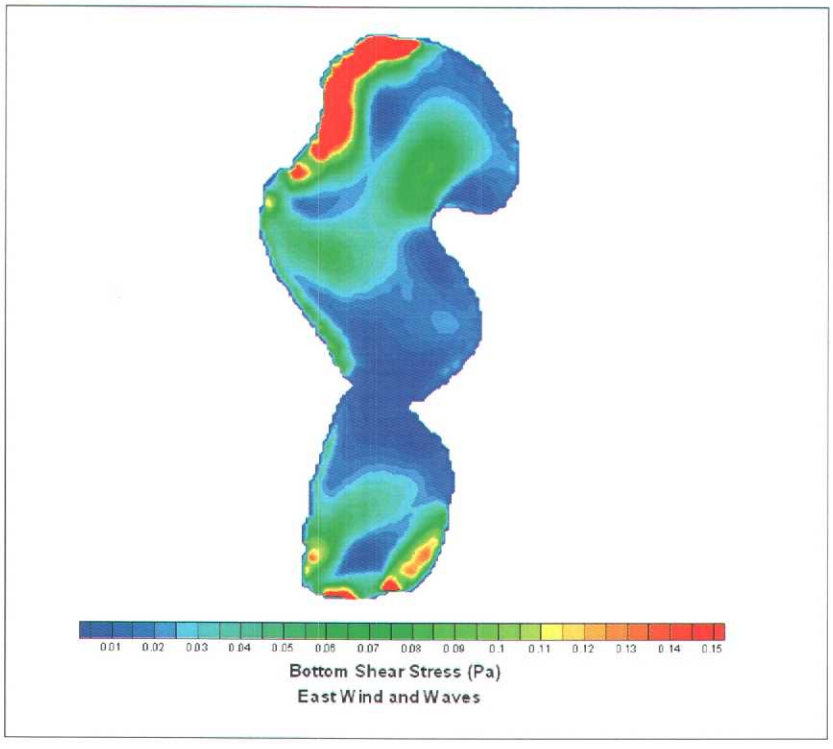

Figure 24: Bottom shear stress contours for an east wind.

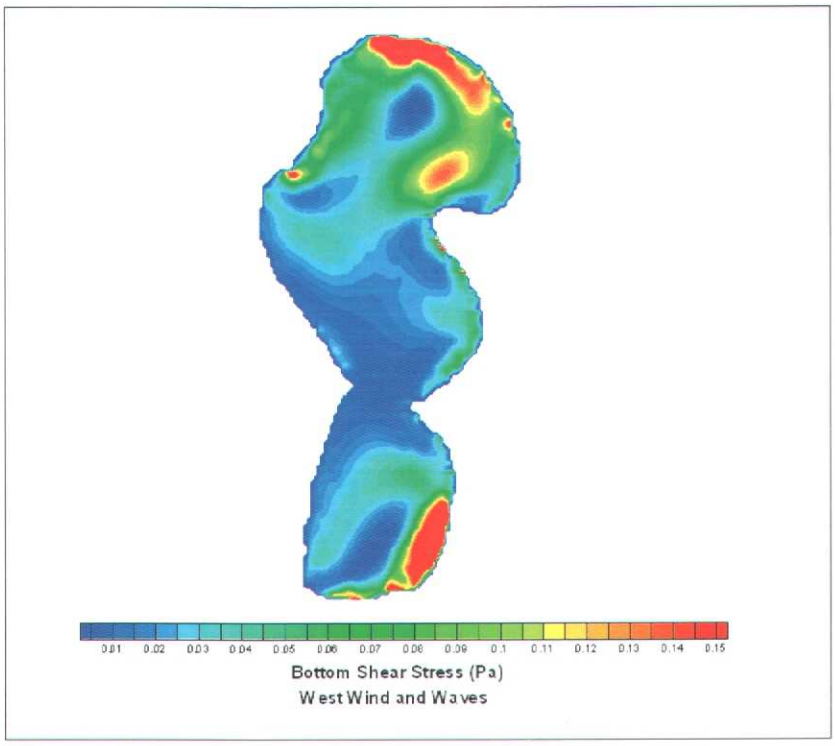

Figure 25: Bottom shear stress contours for a west wind.

Discussion and Conclusions

In summary, with funds provided through the LDRD program, SNL has incorporated the capability to import SEDflume/ASSET Flume-based sediment transport dynamics into EFDC. This was accomplished without losing or removing any of the capabilities of the EFDC model, meaning that all pre-existing formulations are still available within SNL-EFDC, should the user wish to revert to the previous formulation. In essence, SNL-EFDC is the marriage of the two pre-existing model codes; specifically where the sediment and contaminant transport dynamics of SEDZLJ are coupled with the hydrodynamics of EFDC. Work is ongoing to incorporate additional data that may be collected with the ASSET (bedload fraction) and SEAWOLF flumes (oscillatory shear stress erosion data). Through incorporation of data collected with the SEDflume, site-specific erosion and transport data can be used directly in the model rather than basing erosion on outdated or erroneous empirical formulations.

Since the development of SNL-EFDC, the Soil and Sediment Transport Team at SNL has won three WFO grants to: 1) apply SNL-EFDC to a field site; 2) perform similar enhancements to other models; and, 3) assist with a sensitivity analysis using EFDC (not SNL-EFDC). SNL-EFDC is also being used to study the Pecos River and the Nambe Reservoir through funds provided by the SNL Small Business Assistance Program.

References

Abramowitz, M. and I. Stegun, 1972. *Handbook of Mathematical Functions*, National Bureau of Standards, Mathematics Series 55, Washington, D.C.

Bagnold, R.A., 1956. The flow of cohesionless grains in fluids. *Phil. Trans. Royal Soc. London A*, **249**(*964*), 234–297.

Blumberg, A.F. and G.L Mellor, 1987. A description of a three-dimensional coastal ocean circulation model, *In*: N. S. Heaps (ed.), *Three-dimensional Coastal Ocean Models.* Number 4 in *Coastal and Estuarine Sciences*, American Geophysical Union, 1–16.

Borah, D., C. Alonso, and S. Prasad, 1983, Routing graded sediments in streams: Formulations, *J. Hyd. Eng. ASCE*, **108**(*12*), 1486–1502.

Cardenas, M., J. Gailani, C.K. Ziegler, and W. Lick, 1995. Sediment transport in the Lower Saginaw River, *Mar. Fresh. Res.*, **46**, 337–347.

Cheng, N.S., 1997. Simplified settling velocity formula for sediment particle, *J. Hyd. Eng., ASCE*, **123**(*2*), 149–152.

Chroneer, Z., M. Cardenas, J. Lick, and W. Lick, 1995. Sediment and contaminant transport in Green Bay, *Estuarine and Coastal Modeling, Proceedings of the 4th International Conference*, 313–324.

Dwight, H.B., 1961. *Tables of Integrals and Other Mathematical Data*, The MacMillan Company, New York, N.Y.

Engelund, F. and E. Hansen, 1967. *A monograph on sediment transport in alluvial streams.* Teknisk Vorlag, Copenhagen, Denmark.

EPA, 2000. Appendix 3: Theoretical and computational aspects of sediment transport in the EFDC model, EFDC Technical Memorandum, 2nd Draft, *U. S. Environmental Protection Agency, Office of Science and Technology*, 401 M Street SW, Washington, DC.

Fisher, H.B., E.J. List, R.C.Y. Koh, J. Imberger, and N.H. Brooks, 1979. *Mixing in Inland and Coastal Waters*. Academic Press, 483 pp.

Franzini, J.B. and E.J. Finnemore, 1997. *Fluid Mechanics*, 9th ed., McGraw-Hill.

Gailani, J., C.K. Ziegler, and W. Lick, 1991. The transport of sediments in the Fox River, *J. Great Lakes Res.*, **17**, 479–494.

Galperin, B., L.H. Kantha, S. Hassid, and A. Rosati, 1988. A quasi-equilibrium turbulent energy model for geophysical flows. *J. Atmos. Sci.*, **45**, 55–62.

Garcia, M.H., 1999. Ch. 6: Sedimentation and Erosion Hydraulics. *In*: Larry Mays (ed.), *Hydraulic Design Handbook*, McGraw-Hill, 6.1–6.113.

Garcia, M.H. and G. Parker, 1991. Entrainment of bed sediment into suspension. *J. Hyd. Eng. ASCE*, **117**, 414–435.

Gessler, J., 1967. *The Beginning of Bedload Movement of Mixtures Investigated as Natural Armoring in Channels*, W.M. Keck Laboratory of Hydraulics and Water Resources, California Institute of Technology, Translation T-5.

Grant, W. D. and O. S. Madsen, 1979. Combined wave and current interaction with a rough bottom, *J. Geophys. Res.*, **84**, 1797–1808.

Guy, H.P., D.B. Simons, and E.V. Richardson, 1966. *Summary of Alluvial Channel Data from Flume Experiments, 1956-1961*, Geological Survey Professional Paper 462-I, Washington, D.C.

Hamrick, J.M., 1996. User's manual for the environmental fluid dynamics computer code, *Special Report No. 331, Virginia Institute of Marine Sciences*.

Hydroqual, Inc., 1997. *Modeling suspended load transport of non-cohesive sediments in the Hudson River*. General Electric Company, Albany, NY.

Isphording, W.C., E.J. Barclay, and R.J. Barkett, 2003. Sediment particle analysis: Which method is "best?" *Geologic Society of American Annual Meeting Abstracts*, **35**(*1–5*), 58-10.

Jepsen, R., J. McNeil, and W. Lick, 2000. Effects of gas generation on the density and erosion of sediments from the Grand River. *J. Great Lakes Res.*, **26**, 209–219.

Jepsen, R.A., J.D. Roberts, and W. Lick, W., 1997. Effects of bulk density on sediment erosion rates, *Water, Air, and Soil Pollution*, **99**, 21–31.

Jones, C. and W. Lick, 2001. Contaminant flux due to sediment erosion, *Proceedings of the 7th International Conference: Estuarine and Coastal Modeling*, 280–293.

Jones, C. and W. Lick, 2001. Sediment erosion rates: Their measurement and use in modeling, Proceedings of the *Texas A&M Dredging Seminar*, 1–15.

Johnson, B., K. Kim, R. Heath, B. Hsieh, and H. Butler, 1993. Validation of three-dimensional hydrodynamic model of Chesapeake Bay. *J. Hyd. Eng. ASCE*, **119**(*1*), 2–20.

King, I., J.V. Letter, B.P. Donnell, W.H. McAnally, and W.A. Thomas, 2000. SED2D WES Version 4.5, User's Guide. *Engineer Research and Development Center, Waterways Experiment Station, Coastal and Hydraulics Laboratory*, Vicksburg, MS. 174 pp., http://chl.wes.army.mil/software/tabs.

Krone, R. B., 1962. *Flume Studies of the Transport of Sediment in Estuarial Shoaling Processes*, Final Report to San Francisco District, U.S. Army Corps of Engineers, Washington, D.C.

Lick, W. and J. McNeil, 2001. Effects of sediment bulk properties on erosion rates, *Sci. Total Environ.*, **266**, 41–48.

McNeil, J., C. Taylor, and W. Lick, 1996. Measurements of erosion of undisturbed bottom sediments with depth, *J. Hyd. Eng. ASCE*, **122**(*6*), 316–324.

Mellor, G. L. and Yamada, T., 1982. Development of a turbulence closure model for geophysical fluid problems. *Rev. Geophys. Space Phys.*, **20**, 851–875.

Meyer-Peter, E. and R. Müeller, 1948. Formulas for bed-load transport. *Proceedings of the International Association for Hydraulic Structures Research*, Report of Second Meeting, Stockholm, 39–64.

Miller, M.C., I.C. McCave, and P.D. Komar, 1977. Threshold of sediment motion under unidirectional currents. *Sedimentology*, **24**, 507–528

Parker, G., C. Paola, and S. LeClair, 2000. Probabilistic Exner sediment continuity equation for mixtures with no active layer. *J. Hyd. Eng. ASCE*, **126**(*11*), 818–826.

Pender, G., T.B. Hoey, C. Fuller, and I.K. McEwan, 2001. Selective bedload transport during the degradation of a well sorted graded sediment bed. *J. Hyd. Res.*, **39**(*3*), 269–277.

Roberts, J.D., R.A. Jepsen, and S.C. James, 2003. Measurement of sediment erosion and transport with the Adjustable Shear Stress Erosion and Transport Flume. *J. Hyd. Eng. ASCE*, **29**(*11*), 862–871.

Shrestha, P.L., A.F. Blumberg, D.M. DiTorro, and F. Hellweger, F., 2000. A three-dimensional model for cohesive sediment transport in shallow bays. Invited Paper, *ASCE Joint Conference on Water Resources Engineering and Water Resources Planning and Management*.

Soulsby, R.L., 1997. *Dynamics of Marine Sands*, Thomas Telford, London, UK.

Taylor, C. and W. Lick, 1996. Erosion Properties of Great Lakes Sediments, Report, Department of Mechanical and Environmental Engineering, University of California, Santa Barbara, CA 93106.

van Niekerk, A., K. Vogel, R. Slingerland, and J. Bridge, 1992. Routing of heterogeneous sediments over movable bed: model development, *J. Hyd. Eng. ASCE*, **118**(*2*), 246263.

van Rijn, L.C., 1984a. Sediment transport, Part I: Bed load transport. *J. Hyd. Eng. ASCE*, 110(*11*), 1,431–1,436.

van Rijn, L.C., 1984b. Sediment transport, Part II: Suspended sediment transport. *J. Hyd. Eng. ASCE*, **110**(*11*), 1,613–1,641.

van Rijn, L.C., 1984c. Sediment transport, Part III: Bedforms and alluvial roughness. *J. Hyd. Eng. ASCE*, **110**(*11*), 1,733–1,754.

Wikepedia, 2005. http://en.wikipedia.org/wiki/Weighted_geometric_mean, accessed 9/13/2005.

Wu, W., S.Y. Wang, and Y. Jia, 2000. Nonuniform sediment transport in alluvial rivers. *J. Hyd. Res.*, **38**(*6*), 427–434.

Yen, C.-L., 2004. Personal communication, Department of Civil Engineering, National Taiwan University.

Yen, C.-L. and K.T. Lee, 1995. Bed topography and sediment sorting in channel bed with unsteady flow. *J. Hyd. Eng. ASCE*, **121**(*8*), 591–599.

Ziegler, C.K. and B.S. Nisbet, 1995. Long-term simulation of fine-grained sediment transport in large reservoir, *J. Hyd. Eng. ASCE.*, **121**(*11*), 773–781.

Distribution

1	MS 0123	Donna Chavez, LDRD Office, 01011
2	MS 0899	Technical Library, 9616
2	MS9018	Central Technical Files, 8945-1